



## RESEARCH ARTICLE

10.1029/2018JC014122

## Propagation and Vertical Structure of the Tidal Flow in Nares Strait

Peter E. D. Davis<sup>1</sup> , Helen L. Johnson<sup>2</sup> , and Humphrey Melling<sup>3</sup> <sup>1</sup>British Antarctic Survey, Cambridge, UK, <sup>2</sup>Department of Earth Sciences, University of Oxford, Oxford, UK, <sup>3</sup>Institute of Ocean Sciences, Fisheries and Oceans Canada, Sidney, British Columbia, Canada

## Key Points:

- The semidiurnal barotropic  $M_2$  and  $S_2$  tides in Nares Strait are standing waves; the  $K_1$  diurnal tide is a progressive wave traveling northward
- Semidiurnal tidal currents vary strongly with depth, while the diurnal tidal current is depth invariant
- Changes in ellipse shape and/or orientation compared to the along-strait direction allow across-strait flow

## Correspondence to:

P. E. D. Davis,  
petvis@bas.ac.uk

## Citation:

Davis, P. E. D., Johnson, H. L., & Melling, H. (2019). Propagation and vertical structure of the tidal flow in Nares Strait. *Journal of Geophysical Research: Oceans*, 124, 281–301.  
<https://doi.org/10.1029/2018JC014122>

Received 27 APR 2018

Accepted 10 DEC 2018

Accepted article online 15 DEC 2018

Published online 14 JAN 2019

**Abstract** The southward freshwater flux through Nares Strait is an important component of the Arctic's freshwater budget. On short time scales, flow through the strait is dominated by the tides, and tidal dynamics may be important for the magnitude of the freshwater flux over longer periods. Here we build upon our existing knowledge of the tides in the region by exploring their propagation and vertical structure using data from four bottom-mounted Acoustic Doppler Current Profilers deployed in Nares Strait between 2003 and 2006. We observe that propagating barotropic semidiurnal tidal waves interact to create a standing wave pattern, explaining the abnormally large tidal amplitudes that are observed in this region. In the along-strait direction, semidiurnal tidal currents exhibit strong variations with depth. In contrast, the diurnal tides propagate northward through the strait as progressive waves, and the tidal currents are broadly depth invariant. Proximity of Nares Strait to the semidiurnal critical latitude and the topographical restriction imposed by the steep side wall of Ellesmere Island are primary drivers behind the observed vertical variability. In the upper part of the water column, baroclinic activity increases the tidal current amplitude by up to 25%. In the across-strait direction, a two-layer structure exists in both the diurnal and semidiurnal tidal flow, with a phase lag of approximately a quarter of a tidal cycle across the strait for the semidiurnal tide. Our results suggest that strong vertical motion exists against the side walls of Nares Strait, as the across-strait flow interacts with the steeply sloping bathymetry.

**Plain Language Summary** The flow of freshened seawater through Nares Strait, a narrow channel to the west of Greenland, plays an important role in the global climate system. Understanding the processes that are important for setting its strength is therefore critical. The tides in Nares Strait, which are generally much stronger than those found elsewhere in the Arctic Ocean, are one such process. Here we explore how the tides propagate through the region and how their strength varies with depth. We observe that the strong tides result from a standing wave that forms in the center of Nares Strait for the semidiurnal (twice daily) tides, and we show that the strength of these semidiurnal tides varies greatly with depth. In contrast, we see that the strength of the diurnal (once daily) tide is relatively depth invariant. In the across-strait direction, the tides form a two-layer structure, and there is strong vertical flow against the steep side walls of the channel. Our results have important implications for modeling tidal flow in narrow channels such as Nares Strait, and take a vital step toward understanding how the tidal flow affects the freshwater flux through the region.

## 1. Introduction

Nares Strait, a narrow channel to the west of Greenland, forms one of the two major conduits within the Canadian Arctic Archipelago (CAA) through which freshened seawater and sea ice flow from the Arctic Ocean to the North Atlantic (Figure 1a). This freshwater is delivered to the Arctic through a combination of excess precipitation over evaporation, riverine input, and inflow through Bering Strait (Haine et al., 2015; Woodgate, 2018). Variability in the freshwater flux through Nares Strait reflects the changing freshwater content of the Arctic Ocean as well as changes in land ice and sea ice cover (Copland et al., 2007; Rabe et al., 2014; Stroeve et al., 2012). The freshwater is exported directly into the Labrador Sea, where it has the potential to disrupt deep convection and the formation of North Atlantic Deep Water, a key component of the Atlantic Meridional Overturning Circulation. As the Atlantic Meridional Overturning Circulation is responsible for approximately 1 petawatt ( $10^{15}$  W) of northward heat transport at 25°N (e.g., Johns et al., 2011), changes in the export of freshwater through Nares Strait may significantly impact the climate of northwestern Europe. The velocity field in

©2018. The Authors.

This is an open access article under the terms of the Creative Commons Attribution License, which permits use, distribution and reproduction in any medium, provided the original work is properly cited.

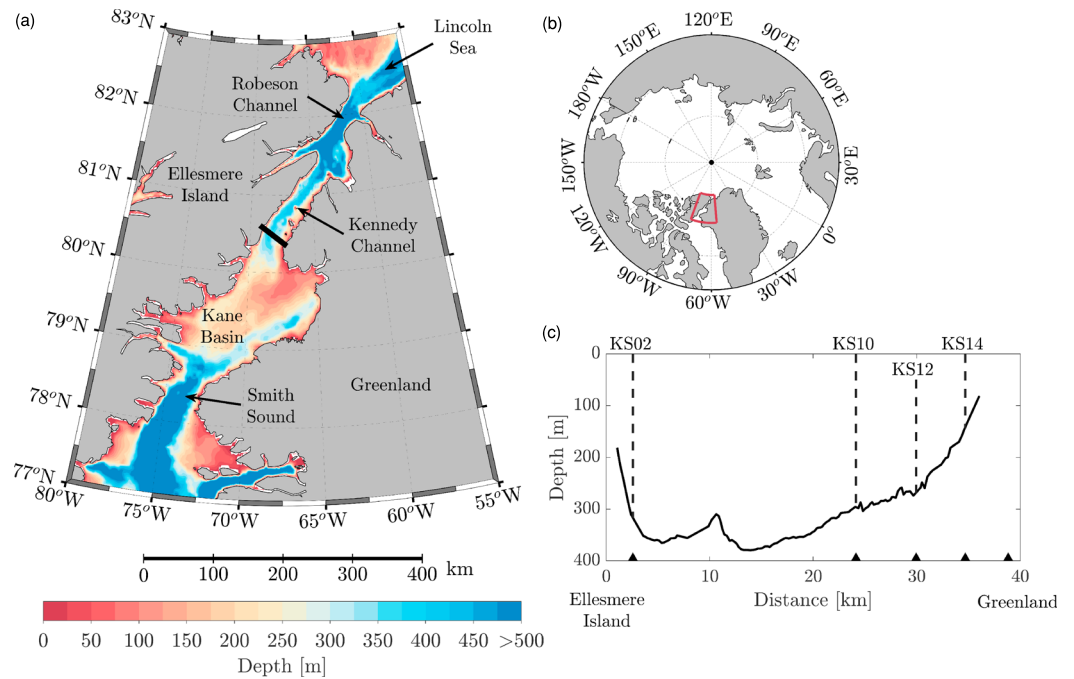


**Figure 1.** (a) Bathymetry of Nares Strait from the International Bathymetric Chart of the Arctic Ocean and (b) its location in the Canadian Arctic Archipelago. The location of the mooring array deployed across Kennedy Channel between 2003 and 2006 is marked with a black line in (a). (c) Cross section looking north through Kennedy Channel at the location of the mooring array showing the observed bathymetry (black solid line) and the positions of the ADCP moorings discussed in this paper.

Nares Strait, however, is dominated by the tides. Indeed, observations show that variability in the strength of the depth-averaged tidal current can exceed variability in the subtidal geostrophic flow by more than 100% (Münchow et al., 2006; Rabe et al., 2012). Therefore, understanding the nature and dynamics of the tide, and any interplay that may exist between the tides and the subtidal flow in the region, is critically important.

Measuring the tidal and oceanic fluxes through Nares Strait is particularly challenging, however (Melling, 2000; Melling et al., 2008). Proximity to the Magnetic North Pole limits the use of the geomagnetic field in providing a reference for flow direction, while the presence of thick sea ice year-round makes access by ship very difficult and presents significant “snagging” hazards to shallow oceanographic moorings. In addition, the internal Rossby deformation radius for the surface freshwater layer is approximately 10 km, much narrower than the “dynamically wide” Nares Strait. Indeed on average, the width of the strait exceeds the deformation radius by a factor of 4 (Münchow et al., 2006; Rabe et al., 2010).

Nevertheless, a long-term monitoring array deployed across Nares Strait between 2003 and 2009 overcame many of these challenges. Using data from this array, Münchow and Melling (2008) showed that, in a depth-averaged sense, the tidal flow is aligned with the along-strait direction and is dominated by the major semidiurnal ( $M_2$  and  $S_2$ ) and diurnal ( $K_1$ ) tidal constituents. The magnitude of these major constituents increases with distance across the strait from Ellesmere Island to Greenland, and the major semidiurnal tides exhibit a greater sense of clockwise rotation. For the lower-frequency subtidal flow, the mean volume transport through Nares Strait between 2003 and 2006 was  $0.71 \pm 0.09$  Sv ( $1 \text{ Sv} \equiv 10^6 \text{ m}^3 \text{ s}^{-1}$ ), increasing to  $1.03 \pm 0.11$  Sv between 2007 and 2009 (Münchow, 2016). The volume flux is driven primarily by the along-channel pressure gradient ( $r^2 = 0.68$ ). Relative to a salinity of 34.8, the liquid freshwater flux reached  $32 \pm 5.7$  mSv between 2003 and 2006, increasing to  $54 \pm 9.3$  mSv between 2007 and 2009. The liquid freshwater flux (i.e., excluding ice) is highly correlated with the total volume transport. Southward advection of ice through the strait adds an additional  $8 \pm 2$  mSv to the total freshwater flux (Münchow, 2016). Overall, the flux of freshwater through Nares Strait accounts for around 45% of all the freshwater that is exported through the CAA (Beszczynska-Möller et al., 2011; Curry et al., 2014).

Sea ice in Nares Strait is typically landfast for several months of the year between January and July, and rapidly drifting during August through December (Agnew, 1998; Samelson et al., 2006). When the sea ice is mobile, local winds contribute to driving the flow through Nares Strait, explaining 60% of the variance in the freshwater flux (Münchow, 2016). The 65% increase in the total freshwater export through Nares Strait between 2003–2006 and 2007–2009 has been attributed to the almost year-round mobile ice conditions seen during the latter period (Münchow, 2016; Shroyer et al., 2015). These year-round mobile ice conditions resulted in a longer period each year during which thick Arctic sea ice was able to flow south through the strait, and strengthened both ice and ocean velocities by increasing the efficiency of atmosphere-ocean momentum transfer (especially during winter when landfast ice would typically isolate the ocean from atmospheric forcing). Surface waters also became fresher as the sea ice flowing south through the strait partially melted during transit (Münchow, 2016). The systematic changes observed between the two periods highlights the important dynamical effect of the sea ice regime in Nares Strait.

In spite of this recent progress, we still know little about the dynamic processes which act to *limit* the volume and freshwater fluxes through the region, and this is hampering our ability to understand to what extent they may be affected by the rapidly changing conditions throughout the Arctic. Possible processes include lateral eddies and friction against the steep side walls of Nares Strait, internal wave drag, turbulence associated with the substantial tidal boundary layers, baroclinic tidal activity, and hydraulic control over the shallow sill in Kane Basin. Here we focus on the region's strong tides. We acknowledge that we cannot directly address how the tidal flow may impact the freshwater flux in Nares Strait due to the lack of hydrographic (temperature and salinity) observations on tidal time scales. Instead, our goal is to build upon the existing depth-averaged analysis of tides by Münchow and Melling (2008) by documenting the vertical structure of the flow through Nares Strait on tidal time scales. This is important as we need to have quantified and understood both tidal and lower-frequency variability in Nares Strait before we can begin to explore how they might interact. In section 3 we examine the nature of tidal propagation in Nares Strait and explain why the tides in this region are particularly strong compared to much of the Arctic Ocean. In sections 4 and 5 we explore the vertical variability of the major tidal constituents and the structure of the across-strait tidal flow, highlighting the considerable variability observed in their magnitude, rotation, and across-strait structure. Finally, we summarize our results in section 6. By developing a fuller understanding of the nature of the tides in the region, we are providing a basis from which future studies can explore the relevant dynamics in more detail, and begin to understand the wider role of the tides in the climatically important freshwater flux through Nares Strait.

## 2. Data and Methods

### 2.1. Kennedy Channel Mooring Array

As part of the long-term monitoring array deployed across Nares Strait between 2003 and 2009, four bottom-mounted 75-KHz Long Ranger Teledyne RD Instruments Acoustic Doppler Current Profilers (ADCPs) were deployed across Kennedy Channel at 80.5°N between 2003 and 2006 (Figure 1). We only use this initial period of the complete 2003–2009 data set here, as this was the limit of the processed data available at the time this study was conducted. The ADCPs made measurements of the average current velocity every half hour over 8-m bins between approximately 15 m above the seabed and 35–40 m from the surface (Münchow & Melling, 2008). All four ADCPs returned complete 3-year data records, with mooring KS02 located 2.6 km from the coast of Ellesmere Island, and moorings KS10, KS12, and KS14 located 14.7, 8.9, and 4.1 km from the coast of Greenland, respectively (Figure 1c). Throughout this paper, the data locations will be primarily referred to by their mooring names.

As ADCPs rely on scatterers in the water column to estimate the current velocity through the Doppler shift, there were periods, primarily during the polar night as well as for short periods each day due to the diel vertical migration, where low scatterer abundance meant it was not possible to determine the current velocity. Velocity data near the surface were also not obtained during periods of significant ice motion (i.e., during the summer and autumn mobile ice period), when the high ambient noise levels drowned out the weaker echoes. In addition, the influence of surface reflections meant that no velocity data could be recovered within the upper 35–40 m of the water column (Münchow & Melling, 2008; Münchow, 2016). Nevertheless, by following the method developed independently by Melling et al. (1995) and Visbeck and Fischer (1995), careful processing of the ADCP data does allow the ice velocity to be recovered and, similar to the approach of Münchow (2016), this can be taken as an estimate of the ocean velocity at the ice-ocean interface. Note that, by definition, the velocity at the ice-ocean interface is zero during landfast ice seasons.

To counter the effect of the proximity of Nares Strait to the Magnetic North Pole, each ADCP was mounted on a torsionally rigid mooring to prevent it from rotating throughout the deployment, and the true geographic heading of the flow was determined after the moorings were recovered. To determine the true heading, observations of the tidal currents taken over several tidal cycles from a ship-mounted ADCP in August 2003 (Münchow et al., 2006) were compared with a barotropic tidal model of the Arctic with a 5-km resolution (Padman & Erofeeva, 2004). Both consistently showed that the depth-averaged tidal current was aligned with the geographic orientation of Nares Strait at the location of the mooring array (30° due east from true north). Thus, the unknown geographic heading was estimated through vector cross-correlation between the barotropic tidal model and the observed velocity at the location of each ADCP (Münchow & Melling, 2008). The along-strait coordinate system throughout this study is defined as 30° due east from true north at all moorings (equivalent to a 60° counterclockwise rotation from due east).

We acknowledge that a spatially varying along-channel direction may be warranted, especially close to Greenland and Ellesmere Island where the orientation of the coastline and/or the bathymetry may become important for steering the flow. However, as it is challenging to define the orientation of these coastal and bathymetric features due to their large range of scales, we have opted to use a fixed definition of the along-channel direction.

To obtain accurate estimates of the phase of the tide at each ADCP, it is necessary to know the exact time basis for each velocity time series. The nominal sampling period was 1,800 s, but the internal clock within each ADCP indicated that the instruments were slow by varying degrees (12 to 33 min) at the end of the deployment. This clock drift was accounted for by assuming it was equally distributed throughout the 3-year deployment, and a slight offset was added to the nominal sampling period for each ADCP before a new set of sample times was generated. Each ADCP also contained a pressure sensor that provided a measurement of the sea bed pressure field on the same time basis as the velocity measurements, and an additional Sea-Bird Electronic SBE37 temperature salinity recorder measured the hydrographic properties at each ADCP with a nominal sampling period of 900 s. Clock drift in these instruments was also accounted for in a similar manner.

## 2.2. Synoptic Hydrographic Sections

In conjunction with the deployment and recovery of the mooring array, full Conductivity, Temperature, and Depth (CTD) hydrographic sections were taken across Nares Strait during the summer of 2003 and on subsequent cruises in the summers of 2007 and 2009 (heavy ice conditions prevented hydrographic sections being taken in 2006). Each individual CTD profile sampled from the surface to the seabed, and the horizontal distance between profiles was typically less than the Rossby deformation radius (2.5–5.0 km).

## 2.3. Ellipse Parameters and Harmonic Analysis

The vertical structure of the tides in Nares Strait was explored by decomposing the ADCP velocity time series into the ellipse parameters associated with each major tidal constituent. Given a time series of orthogonal velocity components  $u$  and  $v$ , a complete complex tidal vector,  $\vec{R}$ , that contains a contribution from all tidal constituents as well as any residual flow, can be constructed (Mooers, 1973):

$$\vec{R} = u + iv. \quad (1)$$

In this complex plane, each individual tidal constituent,  $k$ , that contributes to the full tidal response can be written as the sum of two counterrotating components

$$\vec{R}_k = \vec{R}_k^+ e^{i\omega_k t} + \vec{R}_k^- e^{-i\omega_k t}, \quad (2)$$

where  $\vec{R}_k$  represents the total contribution to the complex tidal vector  $\vec{R}$  from constituent  $k$ ,  $\omega_k$  is the radian frequency of the constituent, and  $t$  is time. The vector addition of these two counterrotating circular vectors defines the shape of a tidal ellipse for each individual tidal constituent. The ellipse represents the path traced by the velocity vector over a period of  $T_k = 2\pi/\omega_k$  and is described by four parameters: the semi-major axis ( $M$ ), the semi-minor axis ( $m$ ), the ellipse inclination ( $\psi$ ), and the phase ( $\phi$ ) (see Mooers, 1973 and Figure 1 in Makinson et al., 2006). The length of the semi-major axis gives the magnitude of the tidal current, while the sign of the semi-minor axis indicates the sense of rotation of the tidal ellipse (positive for counterclockwise rotation in time and negative for clockwise rotation in time). The ellipse inclination angle ( $\psi$ ) gives the orientation of the ellipse and is defined as positive counterclockwise from due east. Therefore, an inclination

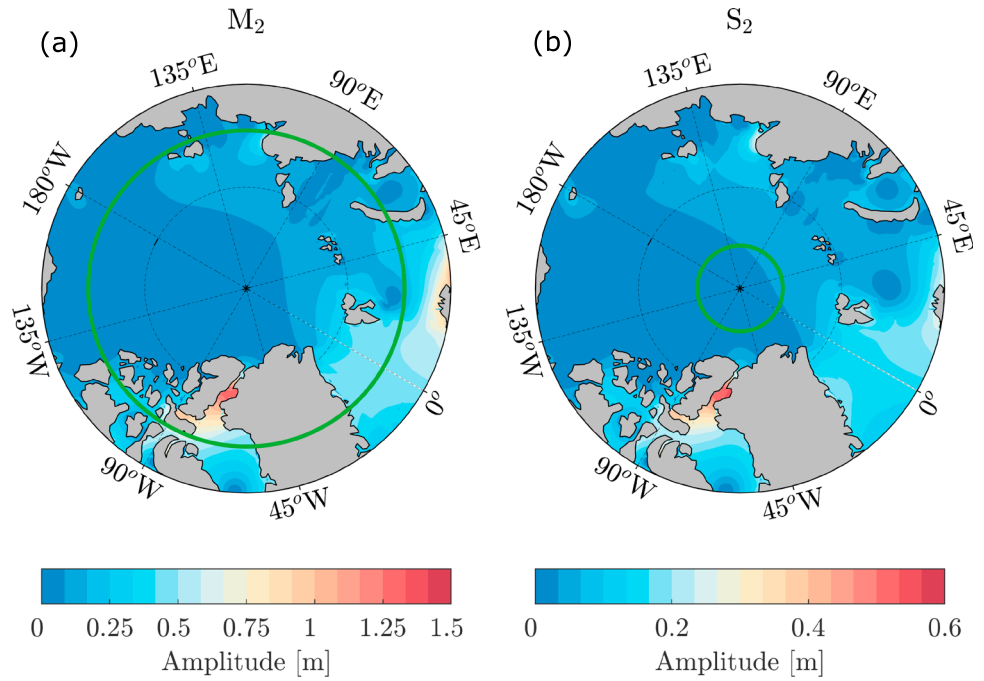


**Figure 2.** Amplitude of the sea level variability associated with (a) the  $M_2$  and (b) the  $S_2$  tide in the Arctic Ocean from the TPX08-atlas tidal model (Egbert & Erofeeva, 2002). Note the different color scales between the  $M_2$  and  $S_2$  tide. The green parallel on each panel marks the location of the critical latitude for the respective tidal constituent.

angle of  $60^\circ$  indicates that the ellipse is aligned with the along-strait direction (defined as  $30^\circ$  due east from true north). The phase ( $\phi$ ) is interpreted as the time lag between an arbitrary reference time and the maximum velocity. Although any reference time can be used, here the astronomical argument correction is used in order to express the phase lags with respect to an absolute time origin. In this way, phase lags for different tidal constituents at different moorings that have different sample times can be directly compared (Foreman & Henry, 1989).

The ellipse parameters for each tidal constituent are found through harmonic analysis (Doodson, 1921; Godin, 1972) using the MATLAB Unified Tidal Analysis and Prediction program (UTide; Codiga, 2011). UTide is a state-of-the-art tidal analysis software package that builds substantially upon the previous work of Foreman, (1977, 1978) and Pawlowicz et al. (2002). UTide determines the ellipse parameters that minimize the difference between the observed and modeled complex tidal vector summed over all  $k = 1, \dots, N$  constituents to be included in the analysis:

$$\vec{R}^{\text{mod}}(t) = \sum_{k=1, \dots, N} (\vec{R}_k^+ e^{iV(t, \omega_k)} + \vec{R}_k^- e^{-iV(t, \omega_k)}) + \vec{R} + \vec{R}.t, \quad (3)$$

where  $\vec{R}$  represents the mean flow ( $\vec{R} = \bar{u} + i\bar{v}$ ),  $\vec{R}$  represents any trend in the data ( $\vec{R} = \dot{u} + i\dot{v}$ ), and  $V(t, \omega_k)$  represents the astronomical argument correction. Any residual between the modeled and observed data is considered to be a signature of the subtidal flow and other random noise in the data set. For long time series, which are dominated by tidal signatures, the random noise and subtidal variability are unlikely to have a significant effect on the estimates of the ellipse parameters. For shorter and/or noisier time series, however, the random noise and sub-tidal variability may have a larger impact. In these cases, a derivative time series smoothed by a 48-hr running mean low-pass filter is subtracted from the velocity records prior to the harmonic analysis, isolating the tidal signature from the lower-frequency variability (i.e., the velocity time series are effectively high-pass filtered, Codiga, 2011).

To quantify the effect of any remaining noise, 95% confidence intervals for the ellipse parameters are calculated. For each tidal constituent included in the harmonic analysis, the complex coefficients  $\vec{R}_k^+$  and  $\vec{R}_k^-$  are used to compute the four corresponding Cartesian cosine/sine coefficients for the  $u$  and  $v$  velocity components. Using these coefficients the variance-covariance matrix is calculated for each individual constituent,

**Table 1***Observed Phase Difference Between Sea Level Variation and Along-Strait Tidal Velocity in Nares Strait at the Location of the Mooring Array*

	KS02	KS10	KS12	KS14
$M_2$	95°	89°	88°	98°
$S_2$	96°	90°	89°	97°
$K_1$	72°	58°	61°	48°

Note. The phase difference represents the lag between the maximum along-strait velocity and the maximum pressure perturbation associated with each tidal constituent.

which are then scaled by the auto- and cross-spectral power of the residuals averaged over the frequency band appropriate for that constituent (Munk et al., 1965). From the scaled variance-covariance matrix and the known cosine/sine coefficients, 200 random realizations of the ellipse parameters for each constituent are generated using Monte Carlo uncertainty propagation. Standard errors of the tidal ellipse parameters are then computed using the median-average-deviation, from which the 95% confidence intervals are calculated. For more details see Codiga (2011), and references therein.

#### 2.4. Barotropic Tidal Model

To aid our investigation into the nature of tidal propagation in Nares Strait, we use output from Version 8 of the Oregon State University TOPEX/Poseidon Global Inverse Solution barotropic tidal model (TPX08-atlas). This is a recent update to the global inverse model described by Egbert and Erofeeva (2002). TPX08-atlas is a global barotropic inverse tidal model which best fits the Laplace tidal equations to along-track-averaged satellite altimeter data (i.e., TOPEX/Poseidon and more recently the Jason satellites), as well as coastal and benthic tide gauges. The model has a  $1/6^\circ$  resolution in the open ocean, increasing to  $1/30^\circ$  in the CAA and other coastal regions. Tidal energy is dissipated at the seabed through a linear drag law, and the loss of energy to the baroclinic tide over regions of steep topography is not accounted for (Egbert & Erofeeva, 2002). The effect of using simple physics in the underlying dynamical model, however, is mitigated by the use of data assimilation (Egbert & Erofeeva, 2002). The bathymetry data used in the areas of interest to this study are a blend of the 2008 version of the global General Bathymetric Chart of the Oceans at one arcminute resolution (Becker et al., 2009), and versions 12.1 and 15.1 of the Smith and Sandwell one arcminute Global Topography (Smith & Sandwell, 1997).

### 3. Tidal Propagation in Nares Strait

Tides in the deep central basin of the Arctic Ocean are generally weak (Figure 2). The amplitude of the sea level variability associated with the major lunar ( $M_2$ ) and solar ( $S_2$ ) semidiurnal tides does not exceed 0.15 m and 0.05 m, respectively (see also Kowalik & Proshutinsky, 1994). In contrast, in the center of Nares Strait, the amplitude of the sea level variability associated with the major semidiurnal tides is an order of magnitude larger (1.2–1.3 m and 0.4–0.5 m for  $M_2$  and  $S_2$ , respectively). No such amplification is seen in the major diurnal tide in Nares Strait ( $K_1$ ; not shown), or in the major semidiurnal tides in other areas of the CAA.

In shallow seas and narrow channels, the barotropic wave associated with each tidal constituent can take a number of different forms. The most common form is a progressive wave, which is characterized by a steady progression of the wave crest, often in the form of a Kelvin wave due to the effect of the Earth's rotation. In a progressive Kelvin wave, the maximum velocity and maximum perturbation in the sea surface height occur at the same time, such that the phase difference between the velocity and the sea surface height variation is zero. A tidal wave can also take the form of a standing wave. A standing wave does not propagate in space but rather oscillates in time around nodes and antinodes. At these points, the constructive and destructive interference of two tidal waves traveling in opposite directions with equal amplitude, phase, and frequency result in the standing wave having a maximum amplitude and zero amplitude, respectively. In a standing wave, the maximum velocity will occur when the perturbation in the sea surface height is zero, such that the phase difference between the two will be  $90^\circ$  (Segar, 2012; Sverdrup et al., 1942).

Given these characteristic phase differences, the nature of the barotropic tidal wave associated with each of the major tidal constituents in Nares Strait can be determined by comparing the phase of the associated pressure perturbation with the phase of the depth-averaged along-strait tidal velocity. For the  $M_2$  and  $S_2$  tidal

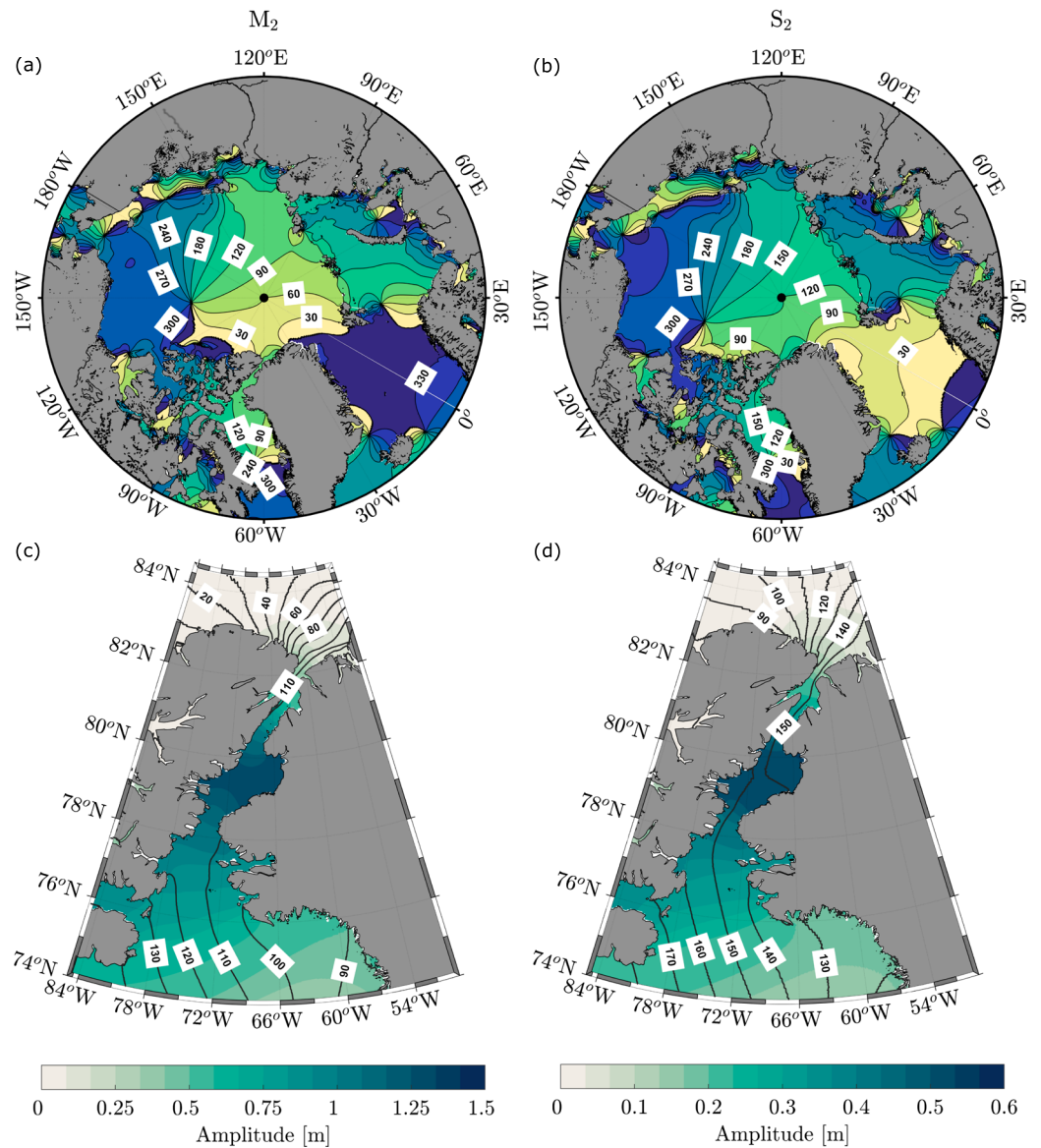


**Figure 3.** Phase in degrees for (a) the  $M_2$  and (b) the  $S_2$  tidal constituent in the Arctic Ocean and Baffin Bay from the TPXO8-atlas tidal model. Amplitude of the sea level variability in meters (colored contours) and phase in degrees (black contours) for (c) the  $M_2$  and (d) the  $S_2$  tidal constituent in Nares Strait from TPXO8-atlas. Note the different color ranges for the amplitude between (c) and (d).

constituents, the phase difference is close to  $90^\circ$  at all ADCPs (Table 1), suggesting that the tidal waves associated with these constituents have standing wave characteristics. Against the coast of Ellesmere Island (KS02) and Greenland (KS14), the phase differences are slightly larger ( $96^\circ$  and  $98^\circ$ , respectively), indicating that lateral friction/proximity to the coastline may be affecting the propagation of the tidal wave. For the  $K_1$  tidal constituent, however, the phase difference is  $60^\circ$  in the center of the strait (KS10 and KS12), increasing to  $72^\circ$  at KS02 and decreasing to  $48^\circ$  at KS14 (Table 1). This suggests that the tidal wave associated with the major diurnal constituent has neither purely progressive nor purely standing wave characteristics.

To explain why the  $M_2$  and  $S_2$  tidal constituents exhibit standing wave characteristics in Nares Strait, we must examine how the barotropic tides propagate to the north in the central Arctic Ocean and to the south in Baffin Bay. The TPXO8-atlas tidal model shows that in the central Arctic Ocean and Baffin Bay, the major semidiurnal tidal waves propagate as progressive waves counterclockwise from their source in the North Atlantic (Figures 3a and 3b; Egbert & Erofeeva, 2002; Kowalik & Proshutinsky, 1994). As a result, two individual tidal waves of equal frequency propagate into Nares Strait: one from the north through Robeson Channel, and one

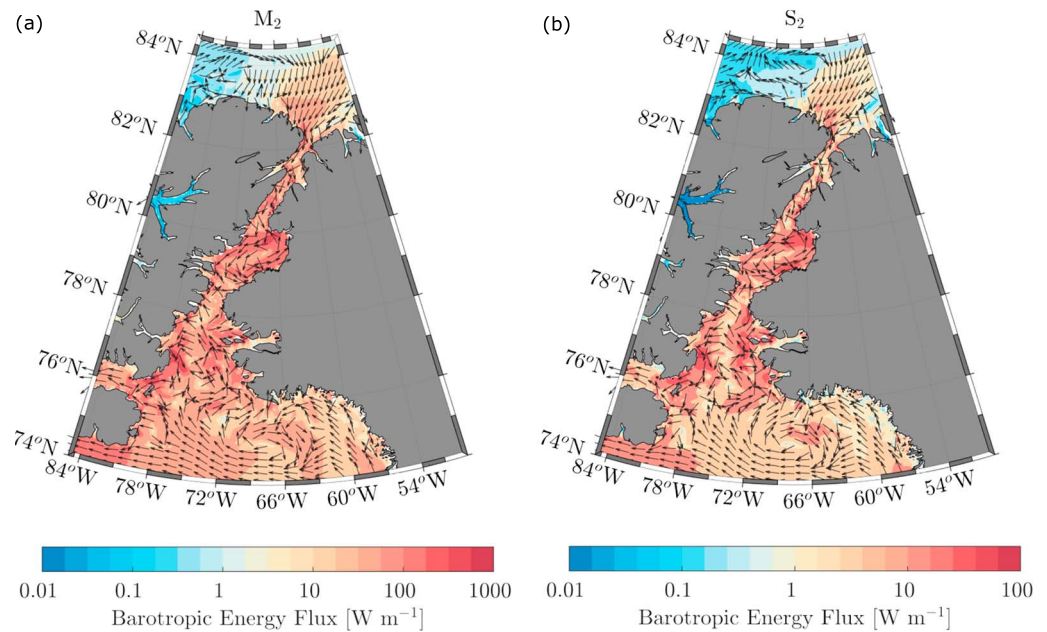


**Figure 4.** Barotropic tidal energy flux from TPX08-atlas for (a) the  $M_2$  and (b) the  $S_2$  tidal constituent in Nares Strait. Colored contours show the magnitude of the energy flux, while the unit vector arrows indicate the direction of the energy flux. Note the different color ranges for the magnitude between (a) and (b).

from the south through Smith Sound. The phase of these tidal waves as they enter Nares Strait is identical ( $110^\circ$  and  $150^\circ$  for the  $M_2$  and  $S_2$  tidal constituents, respectively; Figures 3c and 3d), as is the magnitude of their barotropic tidal energy flux (Figure 4):

$$\bar{P} = \rho gh \langle \vec{u}_{bt} \eta \rangle, \quad (4)$$

where  $\rho$  is density,  $g$  acceleration due to gravity,  $h$  water depth,  $\vec{u}_{bt}$  the barotropic tidal vector,  $\eta$  sea surface displacement, and  $\langle \rangle$  indicates a time average. As these two tidal waves travel through Nares Strait, standing wave characteristics are generated through the constructive interference of the two waveforms, and there is a convergence of tidal energy in Kane Basin (Figure 4) coincident with the location of the largest semidiurnal sea surface height tidal amplitudes (Figures 3c and 3d). Thus, it is the formation of this standing wave that results in the abnormally large semidiurnal tidal amplitudes in Nares Strait compared to the remainder of the CAA and the wider Arctic Ocean (Figure 2). The production of this standing wave, however, is highly dependent on the modern day bathymetry and coastal topography funneling the tidal waves into Nares Strait. In the paleo-past when the bathymetry and coastal topography were significantly altered (e.g., due to an ice sheet blocking the northern end of the strait, or to more subtle changes in the Arctic Ocean and/or Baffin Bay), the tides in this region would have been very different (e.g., Wilmes & Green, 2014).

In contrast, a phase difference exists between the progressive  $K_1$  tidal wave to the north of Nares Strait in the Arctic Ocean (which is formed directly in the Arctic Ocean by the astronomical forcing, rather than being sourced from the North Atlantic, Kowalik & Proshutinsky, 1993; Proshutinsky, 1991), and the  $K_1$  tidal wave to the south of Nares Strait in Baffin Bay (Figure 5a). Consequently, the major diurnal tide in Nares Strait is characterized by the northward progression of a single tidal wave from Baffin Bay to the Arctic Ocean (Figure 5b; the phase increases with latitude), with a south to north flux of tidal energy through the strait (Figure 5c). The lack of constructive interference between two identical waveforms means a standing wave cannot form, and there is no convergence of tidal energy or amplification of the diurnal tide. It is likely that the complex topography and bathymetry of the region are the reasons behind the nonzero phase difference (Table 1). Note that there is a region of enhanced  $K_1$  sea surface height tidal amplitude (0.3 to 0.4 m; Figure 5b) to the south of Smith Sound where Nares Strait meets Baffin Bay (Figure 1). This may be related to formation of shelf waves as the  $K_1$  tide interacts with the nonuniform bathymetry of the continental slope in this region (Kowalik & Proshutinsky, 1993).

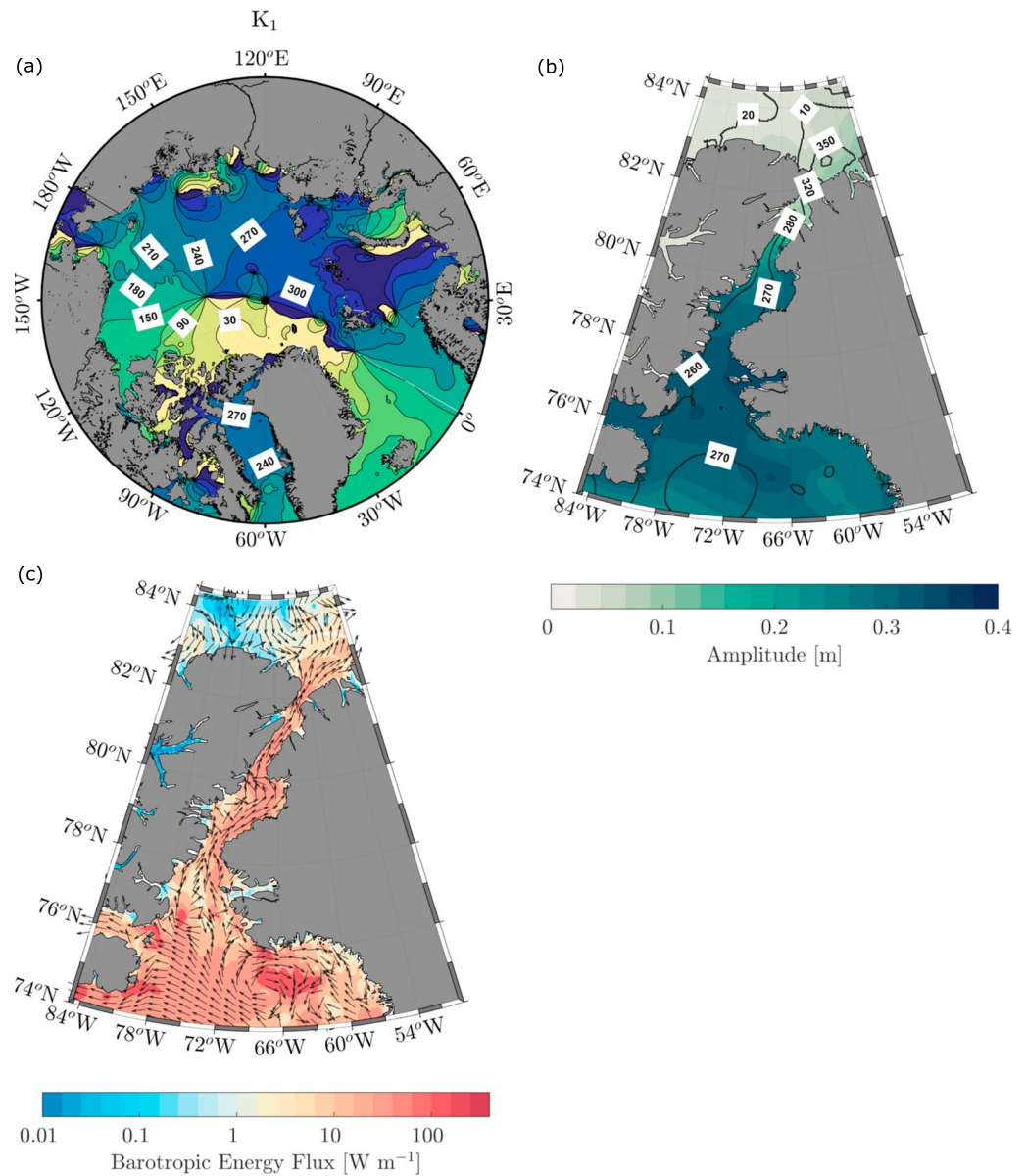


**Figure 5.** (a) Phase in degrees of the  $K_1$  tidal constituent in the Arctic Ocean and Baffin Bay from the TPXO8-atlas tidal model. (b) Amplitude of the sea level variability in meters (colored contours) and phase in degrees (black contours) of the  $K_1$  tidal wave in Nares Strait from TPXO8-atlas. (c) Barotropic tidal energy flux from TPXO8-atlas for the  $K_1$  tidal constituent in Nares Strait. Colored contours show the magnitude of the energy flux while the unit vector arrows indicate the direction of the energy flux. Note the different color range on the amplitude and energy flux panels compared to Figures 3 and 4.

To test the validity of using a barotropic model to investigate tidal propagation through Nares Strait, the average phase difference between sea level variation and along-strait tidal velocity in TPXO8-atlas at the location of the mooring array was examined. The phase differences for the  $M_2$ ,  $S_2$ , and  $K_1$  tidal constituents are identical within the error bars to the observed values (Table 2). Together with the very high level of agreement between the observed cotidal lines in Greisman et al. (1986) and those shown in Figures 3 and 5, this suggests that the TPXO8-atlas model is able to accurately reproduce the nature of the tides in Nares Strait. The previous version of the TPXO model (TPXO7.2), however, cannot accurately reproduce the tidal flow in Nares Strait, drastically underestimating the phase difference for the semidiurnal tides (Table 2). As TPXO7.2 only has a 1/4-degree resolution in the Arctic (compared to the 1/30-degree resolution in TPXO8-atlas), this high-

**Table 2**  
Average Observed and Modeled Phase Difference Between Sea Level Variation and Along-Strait Tidal Velocity in Nares Strait at the Location of the Mooring Array

	Observed	TPX08-atlas	TPX07.2
$M_2$	$93 \pm 5^\circ$	$91 \pm 3^\circ$	$49 \pm 8^\circ$
$S_2$	$93 \pm 4^\circ$	$88 \pm 3^\circ$	$52 \pm 14^\circ$
$K_1$	$60 \pm 10^\circ$	$64 \pm 5^\circ$	$55 \pm 4^\circ$

Note. The phase difference represents the lag between the maximum along-strait velocity and the maximum pressure perturbation associated with each tidal constituent.

lights the importance of using a high-resolution grid to resolve the complex bathymetry when modeling the tides in coastal areas such as Nares Strait (e.g., Chen et al., 2009).

## 4. Vertical Structure of the Tides

### 4.1. Ellipse Semi-major and Semi-minor Axes

The vertical structure of the tidal currents in Nares Strait was examined by harmonically analyzing the full three-year (2003–2006) velocity time series from each depth bin at each ADCP and extracting the ellipse parameters and associated 95% confidence intervals for the  $M_2$ ,  $S_2$ , and  $K_1$  tidal constituents. Together these constituents account for approximately 90% of the total tidal variability. No prefiltering was required to increase the signal-to-noise ratio. Figure 6 shows the vertical structure of the semi-major ( $M$ ; red) and semi-minor ( $m$ ; blue) axes of the tidal ellipse at each ADCP, along with the largest error bars. Each data point represents the average tidal current amplitude over both ice regimes (mobile and landfast), except for the surface data point which is representative of mobile ice seasons only. Note that by harmonically analyzing the full three-year velocity record, we are not considering the possibility of any temporal variability in the vertical structure of  $M$  and  $m$ . Examination of the ADCP velocity records for evidence of temporal variability in the tidal constituents (wide error bars on harmonic fits, differences between consecutive 31-day analyses with inference) has demonstrated, however, that time variation is not an important factor

Against Greenland (KS14; Figure 1c), there is significant variability with depth and between the different tidal constituents. The semi-major and semi-minor axes of the  $M_2$  and  $S_2$  tidal constituents exhibit smooth parabolic-like profiles. For the semi-major axis, the largest values of 30 and 12 cm/s are observed at a depth of 60–70 m for the  $M_2$  and  $S_2$  constituents, respectively, significantly greater than the amplitude of the barotropic tide estimated from the TPX08-atlas tidal model. The amplitude of the semi-major axis decreases toward the surface and bottom boundaries due to friction. As the surface amplitude reflects only mobile ice seasons, it appears that the integrated frictional effect of the various different surface boundary conditions during these seasons (open sea, pack ice in free drift, and pack ice retarded by ice stress) has a noticeable impact on the amplitude of the tidal current at the surface.

The largest semidiurnal tidal amplitudes coincide with an increasingly negative semi-minor axis, indicating that the semidiurnal tidal ellipses exhibit a greater sense of clockwise rotation in time with distance from the top and bottom boundaries. At the top and bottom boundaries, the semi-minor axis is close to zero or even slightly positive indicating counterclockwise rotation. However, even at the depth of maximum rotation (60 m), the ellipse eccentricity (ratio of the semi-minor axis to the semi-major axis) is still less than 0.2. This indicates that the ellipse is still highly elongated and much closer to being rectilinear than circular (see Figure 8 in Münchow & Melling, 2008). These low levels of eccentricity for the semidiurnal tides are consistent throughout Nares Strait. The diurnal constituent ( $K_1$ ) at KS14 is comparatively depth-invariant away from the boundaries, except for a small peak in the semi-major axis of 17 cm/s at 105 m. The semi-minor axis and ellipse eccentricity are near zero everywhere, indicating that the  $K_1$  tidal ellipse close to Greenland is rectilinear.

Unlike the variability seen between constituents at KS14, the three major tidal constituents at KS02 (adjacent to Ellesmere Island; Figure 1c) all show broadly the same vertical structure. The amplitude of the semi-major axis increases with distance from the seabed, reaching an observed maximum at 50 m of 13, 5, and 7 cm/s, for the  $M_2$ ,  $S_2$ , and  $K_1$  tides, respectively (the tidal current amplitude may continue to increase in the unobserved portion of the water column). The semi-minor axis for all constituents is close to zero everywhere, indicating that both the diurnal and semidiurnal tidal flow against the coast of Ellesmere Island is largely rectilinear. This

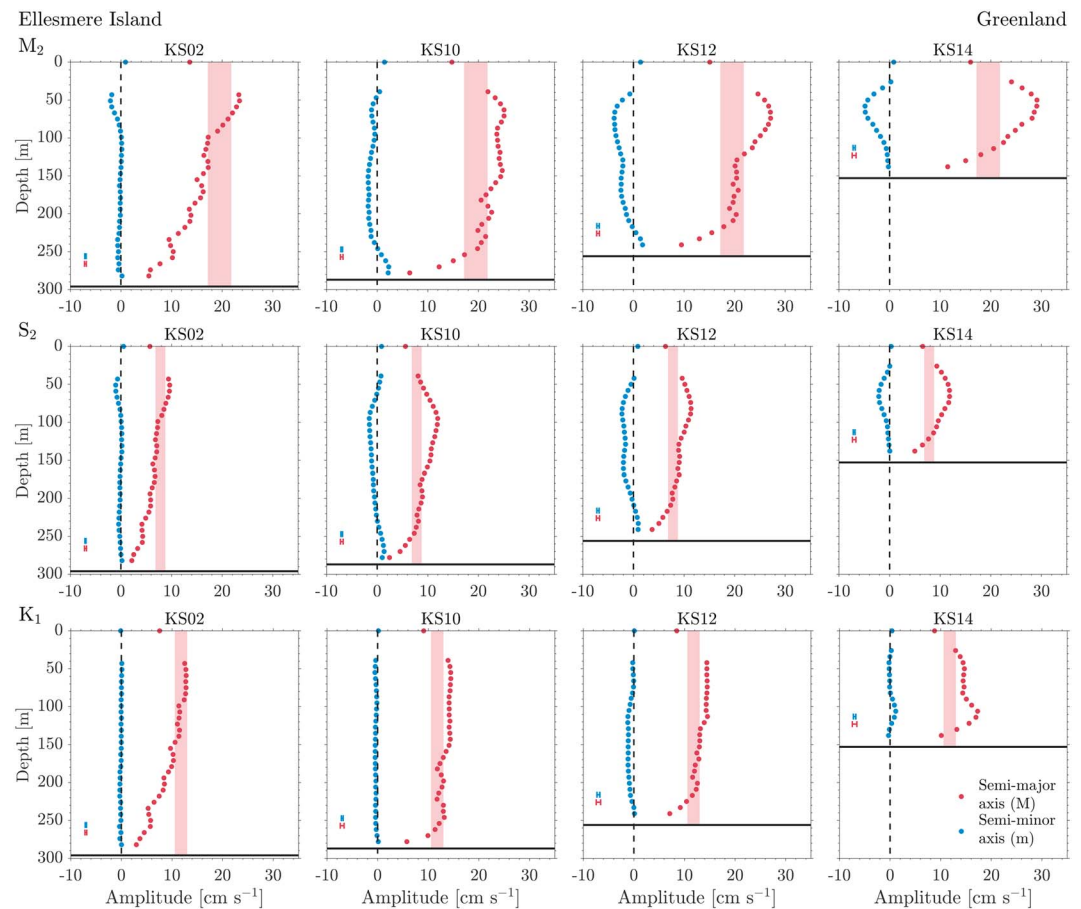


**Figure 6.** Vertical structure of the semi-major ( $M$ ; red) and semi-minor ( $m$ ; blue) axes of the tidal ellipse for the  $M_2$  (top row),  $S_2$  (middle row), and  $K_1$  (bottom row) tidal constituents at KS02 (left column), KS10 (middle-left column), KS12 (middle-right column), and KS14 (right column). Each data point represents the average tidal current amplitude over both ice regimes in Nares Strait (mobile and landfast), except the surface point which is representative of only mobile ice periods. Semi-minor (blue) data points that lie to the left of the black dashed line in each panel (zero line) indicate clockwise rotation (i.e., a negative semi-major axis), while semi-minor data points that lie to the right of the black dashed line indicate counterclockwise rotation (i.e., a positive semi-major axis). The confidence intervals are generally smaller than the individual data points. The largest confidence interval for both the semi-major and semi-minor axes is plotted in each panel. The pale red bars indicate the average amplitude of the barotropic tidal current ( $\pm 1$  standard deviation) at the location of the mooring array from the TPX08-atlas tidal model, and the solid black line in each panel marks the depth of the seabed at that mooring.

is in contrast to the rotational nature of the semidiurnal tides observed close to Greenland. In the upper 100 m, the semidiurnal tidal ellipses do exhibit a tendency toward clockwise rotation ( $m < 0$ ).

At KS10 and KS12 (15 and 10 km from the coast of Greenland, respectively; Figure 1c), the amplitude of the  $K_1$  semi-major axis increases rapidly with distance from the seabed, quickly reaching an amplitude equal to that of the barotropic tide estimated from TPX08-atlas. In contrast, the amplitudes of the semidiurnal semi-major axes increase more slowly with distance from the seabed and exhibit thicker boundary layers. In the upper half of the water column, the semi-major amplitudes of both the diurnal and semidiurnal tides tend to become greater than the amplitude of the barotropic tide estimated from TPX08-atlas. The result is that an upper water column maximum in the amplitude of all the major tidal constituents exists across Nares Strait, although it is clearer in the semidiurnal tides. The semi-minor axis of the  $M_2$  and  $S_2$  tides is generally negative throughout the water column (i.e., exhibiting the same clockwise rotation as seen at KS14), but becomes slightly positive close to the top and bottom boundaries. In contrast, the semi-minor axis of the  $K_1$  tide is close to zero throughout the water column at both KS10 and KS12, mirroring the same rectilinear nature of the  $K_1$  tide that is observed against each coast.

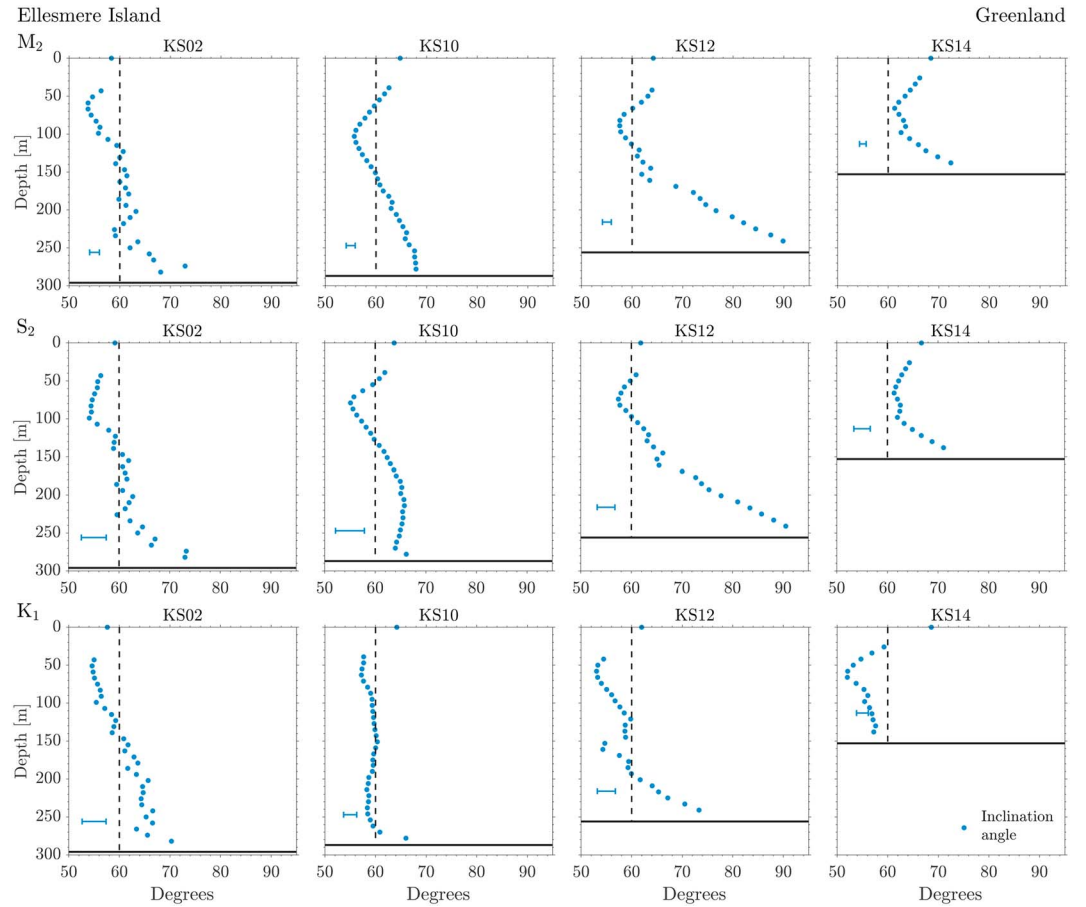


**Figure 7.** Vertical structure of the tidal ellipse inclination angle ( $\psi$ ) for the  $M_2$  (top row),  $S_2$  (middle row), and  $K_1$  (bottom row) tidal constituents at KS02 (left column), KS10 (middle-left column), KS12 (middle-right column), and KS14 (right column). Each data point represents an average of both ice regimes in Nares Strait (mobile and landfast), except the surface point which is an average of only mobile ice periods.  $\psi$  is defined as positive counterclockwise from due east, and therefore an inclination angle of  $60^\circ$  (black dashed line) indicates that the tidal ellipse is aligned with the local along-strait orientation (defined  $30^\circ$  due east from true north). The confidence intervals are generally smaller than the individual data points. The largest confidence interval is plotted in each panel. The solid black line in each panel marks the depth of the seabed at that mooring.

Although a full investigation of the dynamics that set the observed vertical structure of the tides is beyond the scope of this study, a number of inferences can be drawn about the processes that are likely to be important. The characteristic boundary layer depth ( $\delta^+$  and  $\delta^-$ ) for each of the rotary components that make up the tidal ellipse ( $\vec{R}_k^+$  and  $\vec{R}_k^-$ ; equation (2)) is given by

$$\delta^+ \approx \left( \frac{2K_m}{|\omega + f|} \right)^{\frac{1}{2}} \quad (5)$$

and

$$\delta^- \approx \left( \frac{2K_m}{|\omega - f|} \right)^{\frac{1}{2}}, \quad (6)$$

where  $K_m$  is the eddy viscosity, and  $|\omega \pm f|$  is the sum or difference between the tidal frequency and the local rate of rotation given by the planetary vorticity,  $f$ . The mooring array lies within a latitude band that is bounded by the critical latitudes for the  $M_2$  ( $74^\circ 28.30'N$ ; Figure 2a) and  $S_2$  ( $85^\circ 45.90'N$ ; Figure 2b) tides, where the frequency of the tidal constituent ( $\omega$ ) is equal to the Coriolis frequency ( $f$ ), and  $|\omega - f|$  tends to zero. Therefore, at these latitudes, boundary layer friction and resonant enhancement of the clockwise rotary component ( $\vec{R}_k^-$ ) drives a strong depth dependence in the amplitude of the semidiurnal tides (i.e., large semidiurnal tidal boundary layers) and generates counterclockwise rotation near the boundaries and clockwise rotation in the

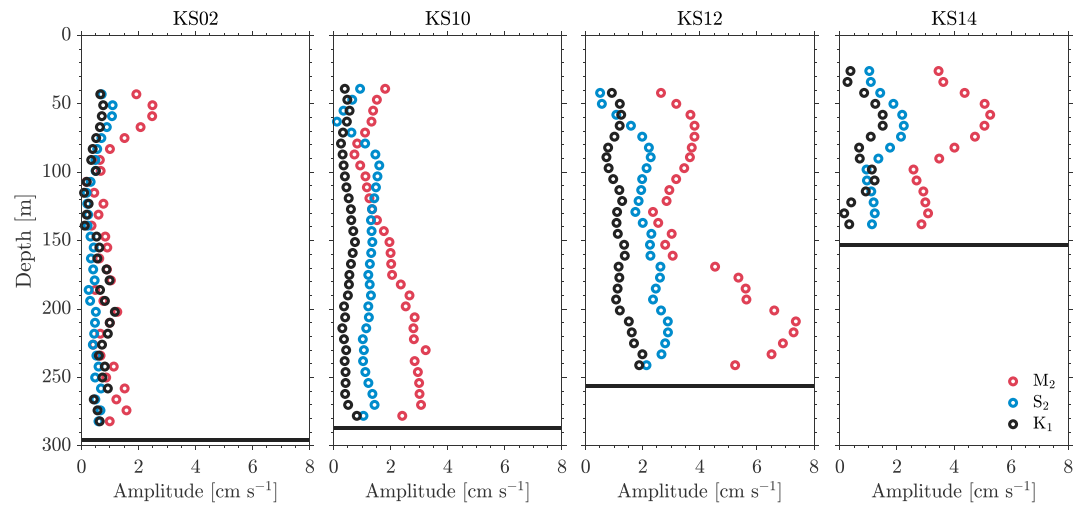


**Figure 8.** Amplitude of the across-strait tidal flow derived from a three-year harmonic analysis at KS02 (left), KS10 (middle-left), KS12 (middle-right), and KS14 (right) for the  $M_2$  (red),  $S_2$  (blue), and  $K_1$  (black) tidal constituents. The black solid line in each panel marks the depth of the seabed at that mooring.

interior. In contrast, assuming that the diurnal tide propagates as a Kelvin wave rather than a shelf wave, diurnal tides are expected to be largely barotropic (i.e., small diurnal tidal boundary layers) and rectilinear in nature as  $f$  is almost twice as large as  $\omega$  (Foldvik et al., 1990, 2001; Makinson et al., 2006; Prandle, 1982; Prinsenber & Bennett, 1989; Robertson, 2005). Note that as lateral shear can generate time-dependent relative vorticity that will modify the local rate of rotation given by the planetary vorticity alone (i.e., the denominator in equations (5) and (6) becomes  $|\omega \pm (f + \zeta)|$ , where  $\zeta$  is the relative vorticity), the depth of the different boundary layers may be time dependent.

Aspects of this variability are clearly observed in Nares Strait (Figure 6), leading us to conclude that critical latitude effects are one of the primary drivers behind the observed vertical variability. The  $K_1$  tide is broadly rectilinear and depth-invariant with small tidal boundary layers. The amplitude of the  $K_1$  semi-major axis quickly reaches the amplitude of the barotropic tide as estimated from the TPX08-atlas tidal model. In contrast, the semidiurnal tides have substantially thicker tidal boundary layers, and show much greater variability in the vertical. In addition, they also exhibit a strong sense of clockwise rotation in the interior ( $m < 0$ ) and counterclockwise rotation ( $m > 0$ ) near the seabed. At KS02, however, the vertical structure of the tides is very different to what would be expected from critical latitude theory. All the major tidal constituents show broadly the same vertical structure, and this is likely related to the topographical restrictions placed on the flow by the steep side wall of Ellesmere Island (12% gradient compared to 3% against Greenland).

Outside of the tidal boundary layers, the amplitude of the semi-major axes tend toward an upper water column maximum (and are generally greater than the magnitude of the barotropic tide estimated from TPX08-atlas; Figure 6). In this region of the water column, stratification is strong (Rabe et al., 2010). If it is assumed that tidal flows can be decomposed into a barotropic component, a phase-coherent baroclinic component, and a phase-incoherent baroclinic component (Cummins et al., 2001; Dushaw et al., 1995; Kulikov et al., 2010), then this amplification is likely to be a result of baroclinic processes. Ellipse parameters derived from the least squares method of harmonic analysis include a contribution from both the barotropic component and the coherent baroclinic component. Therefore, if we compare the results of harmonic analysis at depths around 200 m where stratification is weak and the phase-coherent baroclinic component is small, with results from depths where stratification is strong and the phase-coherent baroclinic component is large (50 to 100 m), we can derive an estimate of the importance of the coherent baroclinic component (Kulikov et al., 2010). For the  $M_2$  tide, phase-coherent baroclinic activity increases the average magnitude of the tidal currents by 13–25% at KS10 and KS12, and by 23–26% for the  $S_2$  tide at the same mooring locations. For the  $K_1$  tide at KS10 and KS12, the contribution from coherent baroclinic activity decreases to 13–14%. At KS02 and KS14 it is harder to define a depth range where the amplitude of the tide is relatively depth invariant, stratification is weak, and the phase-coherent baroclinic component is small. Therefore, we do not estimate the contribution of the baroclinic component at these mooring locations. Understanding what controls the magnitude of the

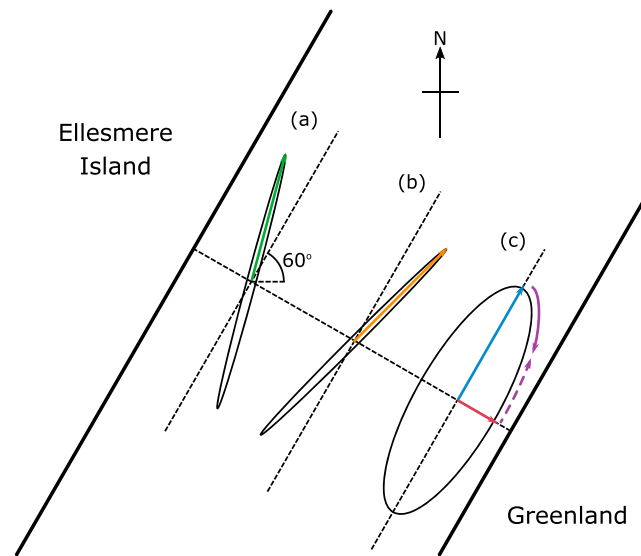


**Figure 9.** Schematic showing the different mechanisms through which an across-strait tidal flow can occur: rotation of the tidal ellipse away from the along-strait direction ( $60^\circ$ ; a, b), or a “fattening” of the tidal ellipse (c). (a) A rectilinear tidal ellipse (characteristic of the tidal flow against Ellesmere Island or the  $K_1$  tide throughout Nares Strait) with an inclination angle greater than  $60^\circ$ . When the along-strait flow toward the Arctic is at a maximum (green arrow), the across-strait flow is at a maximum toward Ellesmere Island ( $180^\circ$  phase difference). (b) A rectilinear tidal ellipse with an inclination angle less than  $60^\circ$ . When the along-strait flow toward the Arctic is at a maximum (orange arrow), the across-strait flow is at a maximum toward Greenland ( $0^\circ$  phase difference). (c) A “fat” tidal ellipse with a small but nonzero semi-minor axis (characteristic of the semidiurnal tides away from Ellesmere Island) and an inclination angle aligned with the along-strait direction. When the along-strait flow toward the Arctic is at a maximum (blue arrow), there is no across-strait flow. For clockwise rotation (purple arrow), the maximum across-strait flow toward Greenland (red arrow) lags the maximum along-strait flow by  $90^\circ$ . For counterclockwise rotation at the boundaries (dashed purple arrow), the maximum across-strait flow toward Greenland leads the maximum along-strait flow by  $90^\circ$ .

baroclinic activity in the upper water column, and why it is in phase with the barotropic component, is worthy of investigation. Answering these questions, however, lies beyond the scope of this present study.

#### 4.2. Ellipse Inclination Angle

Figure 7 shows the vertical structure of the ellipse inclination angle at each ADCP. Although in a depth-averaged sense the mean inclination angle of approximately  $60^\circ$  (defined as positive counterclockwise from due east) indicates that the tidal flow is aligned with the along-strait direction (defined as  $30^\circ$  due east from true north; Münchow & Melling, 2008), significant variability exists with depth and between the different ADCPs. For many ADCPs and tidal constituents, the inclination angle is greater than  $60^\circ$  in the lower half of the water column, reaching a maximum at the bottom boundary. In the upper half of the water column, the inclination angle is generally less than  $60^\circ$ , with a minimum observed between 50 and 150 m. At KS12, the inclination angle reaches an extreme maximum of  $90^\circ$  at the seabed. At KS02 there is less evidence of a minimum in the inclination angle between 50 and 150 m, and instead the inclination angle generally increases with depth for all constituents.

#### 4.3. Summary

In summary, the amplitude of the semidiurnal tides ( $M_2$  and  $S_2$ ) in Nares Strait is highly depth dependent, while the diurnal tide ( $K_1$ ) is broadly depth invariant. The exception is against the coast of Ellesmere Island, where all the major tidal constituents show the same vertical structure. Away from Ellesmere Island (KS10, KS12, and KS14) the semidiurnal tidal current vectors exhibit predominantly clockwise rotation in time, except near the top and bottom boundaries where the rotation becomes counterclockwise. For the diurnal tides and all constituents against the coast of Ellesmere Island, the tidal current vector is largely rectilinear. An upper water column maximum in the amplitude of both the diurnal and semidiurnal tides is seen across Nares Strait, although this feature is clearer in the semidiurnal tides. This upper water column maximum is associated with phase-coherent baroclinic activity.

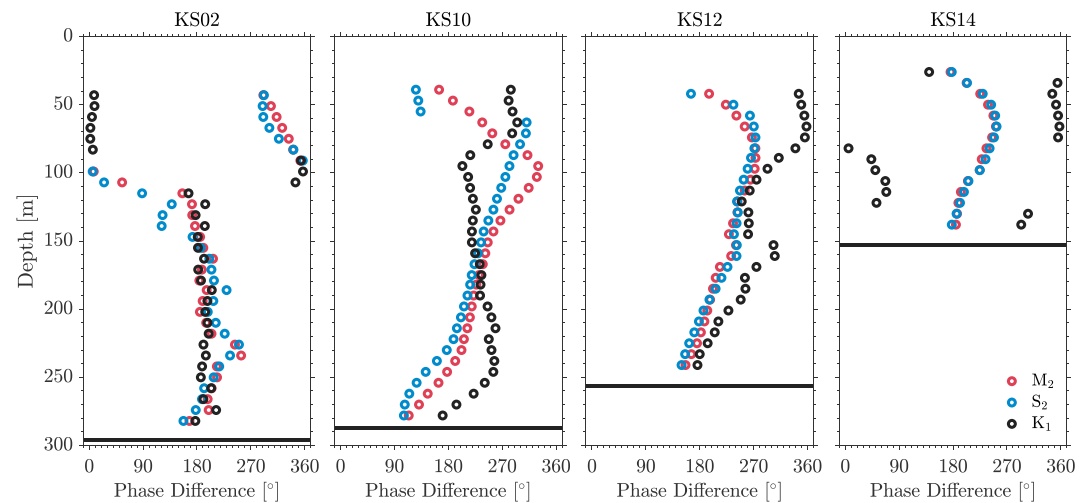


**Figure 10.** Phase difference between the maximum along-strait velocity and the maximum across-strait velocity wrapped to a range of 0–360° at KS02 (left), KS10 (middle-left), KS12 (middle-right), and KS14 (right), for the  $M_2$  (red),  $S_2$  (blue), and  $K_1$  (black) tidal constituents. A phase difference of 180° or 0° indicates that the maximum in the across-strait velocity is antiphased with or in phase with the maximum along-strait velocity, respectively, and is associated with a rotation of the tidal ellipse away from the along-strait direction driving the across-strait flow. A phase difference of 90° or 270° indicates that the maximum in the across-strait velocity leads or lags the maximum along-strait velocity by 90°, respectively, and the across-strait flow is driven by counterclockwise or clockwise rotation of the tidal current vector. The solid black line in each panel marks the depth of the seabed at that mooring.

## 5. Structure of the Across-Strait Tidal Flow

### 5.1. Amplitude, Mechanisms, and Vertical Motion

The structure of the across-strait tidal flow in Nares Strait also differs considerably between moorings. Against the coast of Ellesmere Island (KS02), the amplitude of the across-strait tidal flow below 100 m—where the tidal ellipses are generally rectilinear—is approximately the same for each of the major tidal constituents (Figure 8). Above 100 m, where the semidiurnal tides (especially  $M_2$ ) exhibit clockwise rotation, the amplitude increases to a maximum of 2.5 cm/s. In contrast to the  $K_1$  tide, which exhibits a relatively constant across-strait tidal flow amplitude throughout Nares Strait (black dots in Figure 8), the across-strait amplitude of the  $M_2$  and  $S_2$  tides (red and blue dots in Figure 8) increases across the strait toward the coast of Greenland.

Two mechanisms exist through which an across-strait tidal flow can occur: rotation of the tidal ellipse away from the along-strait direction (which for Nares Strait is 60°; Figures 9a and 9b), or a fattening of the tidal ellipse (i.e., a large semi-minor axis; Figure 9c) such that for periods of each tidal cycle the tidal vector has an across-strait component. The maximum across-strait flow associated with *rotation* of the tidal ellipse will occur when the along-strait flow is at a maximum (green and orange arrows in Figures 9a and 9b). In contrast, the maximum across-strait flow associated with a *fattening* of the tidal ellipse (red arrow in Figure 9c) will occur when the along-strait flow is at a minimum. Thus, by examining the phase difference between the maximum along-strait flow and the maximum across-strait flow, it is possible to determine the primary mechanism through which the across-strait tidal flow occurs. Both mechanisms can of course operate together: the inclination angle of an ellipse with a nonzero semi-minor axis can deviate from the along-strait direction. In this case the phase difference will only indicate which mechanism dominates.

In the case of a purely barotropic tide with rectilinear tidal ellipses aligned with the along-strait direction (such as the diurnal  $K_1$  tide throughout Nares Strait; Figure 6), across-strait tidal flow is strictly limited to the Ekman layer. In Nares Strait an Ekman layer is formed at both the seabed, and at the sea surface under sluggishly drifting pack ice during mobile ice seasons and stationary pack ice during fast ice seasons. These two Ekman layers generate a two-layer across-strait diurnal tidal flow, which is clearest at KS02, KS10, and KS12. Close to the seabed at these locations, the phase difference between the maximum along-strait diurnal flow and the maximum across-strait diurnal flow is close to 180° (Figure 10, black dots). This indicates that the maximum across-strait flow toward Ellesmere Island (defined as negative) coincides with the maximum northward along-strait flow (defined as positive), and thus the across-strait flow occurs predominantly through a rotation of the tidal ellipse toward Ellesmere Island (i.e., ellipse inclination angles >60°; Figure 9a). The ellipse

**Table 3***Average Vertical Displacement Over the Period of the Diurnal and Semidiurnal Tidal Constituents at KS02, KS10, KS12, and KS14*

	$M_2$	$S_2$	$K_1$
KS02	$16.4 \pm 0.0$ m	$5.6 \pm 0.0$ m	$15.5 \pm 0.8$
KS10	$4.9 \pm 0.8$ m	$2.5 \pm 0.8$ m	$6.8 \pm 0.1$
KS12	$11.3 \pm 2.4$ m	$4.7 \pm 0.1$ m	$12.1 \pm 2.0$
KS14	$9.4 \pm 2.6$ m	$3.3 \pm 1.1$ m	$0.5 \pm 0.1$

Note. An uncertainty of  $\pm 0.0$  m indicates that the amplitude of the displacement derived independently from the temperature and salinity time series agree to within 0.01 m.

rotation and the antiphasing between the velocity components is consistent with Ekman transport in the bottom boundary layer. Close to the sea surface, the diurnal phase difference tends toward  $0^\circ$  (Figure 10). This indicates that the maximum positive along-strait flow coincides with the maximum positive across-strait flow toward Greenland (Figure 9b), and is consistent with across-strait flow in an under-ice Ekman boundary layer (i.e., ellipse inclination angles  $<60^\circ$ ; Figure 7).

Our knowledge of the Ekman depth in Nares Strait is speculative as it depends on the poorly constrained eddy viscosity. However, based on the modeling work of Shroyer et al. (2015) and Huntley and Ryan (2018), it likely ranges from 20 to hundreds of meters depending on the strength of the stratification. This range is consistent with our observations. The thickest Ekman layer is observed below 100 m at KS02. Here the interaction of the bottom Ekman layer with the steeply sloping side wall of Ellesmere Island likely results in the Ekman effects propagating far into the water column.

Similar Ekman layer behavior is also exhibited by the semidiurnal tides below 100 m at KS02. Here the proximity to the sloping side wall constrains the tidal ellipses to be close to rectilinear, and the phase difference is close to  $180^\circ$ . Thus, the across-strait flow occurs through a rotation of the tidal ellipse toward Ellesmere Island. For the semidiurnal tides throughout the remainder of Nares Strait (and above 100 m at KS02), however, their baroclinic characteristics become important, and the pattern of across-strait flow diverges from that expected in a purely barotropic ocean. The phase difference tends toward either  $270^\circ$  in the region of the upper water column maximum, or  $90^\circ$  at the boundaries, commensurate with the fattening of the semidiurnal tidal ellipses and the nonzero semi-minor axes observed at these locations. A phase difference of  $270^\circ$  is consistent with the clockwise rotation seen in the region of the upper water column maximum (negative semi-minor axes in Figure 6), with the maximum positive across-strait flow toward Greenland lagging the maximum positive along-strait flow by  $90^\circ$  (Figure 9c). In contrast, a phase difference of  $90^\circ$  corresponds with the trend toward counterclockwise rotation of the semidiurnal tidal current vector near the boundaries (the maximum positive across-strait flow leads the maximum positive along-strait flow; positive semi-minor axes in Figures 6 and 9c).

This pattern of across-strait flow is consistent with critical latitude theory (Prandle, 1982), but might also be related to the coastal geometry found close to Greenland (Figure 1). Here Nares Strait swings through  $60^\circ$  to tend southward at Cape Jefferson 1 km south of the mooring array, while to the north, Franklin and Crozier islands obstruct one third of the channel width within 20 km of the array. As a result, the directions of the flood and ebb tide may not be directly opposite on the Greenland side of the strait, creating "fatter" tidal ellipses compared to the Ellesmere side. Two notable exceptions to the pattern of across-strait flow for the semidiurnal tides away from Ellesmere Island are found near the seabed at KS12 and KS14 (Figure 10). Here the phase difference is close to  $180^\circ$ , and at KS12 is likely due to the extreme inclination angles observed at the seabed dominating the across-strait flow (perhaps as a result of the topographic steering discussed above; Figure 7).

Lateral convergence or divergence in the across-strait tidal flow will drive vertical motion at tidal frequencies. The magnitude of this vertical motion can be calculated by harmonically analyzing the 3-year temperature and salinity time series recorded at each of the ADCPs and dividing the resulting amplitudes by the average vertical temperature and salinity gradients at the seabed derived from the summer CTD sections. A running mean is subtracted prior to the analysis in order to remove all subtidal variability in the temperature and salinity records with periods longer than 48 hr. The vertical motion for any individual tidal constituent (Table 3) is greatest at KS02, followed by KS12. This corresponds to the two regions that we have observed in Nares Strait that exhibit the greatest convergence and divergence. We postulate that the vertical motion at KS02 is

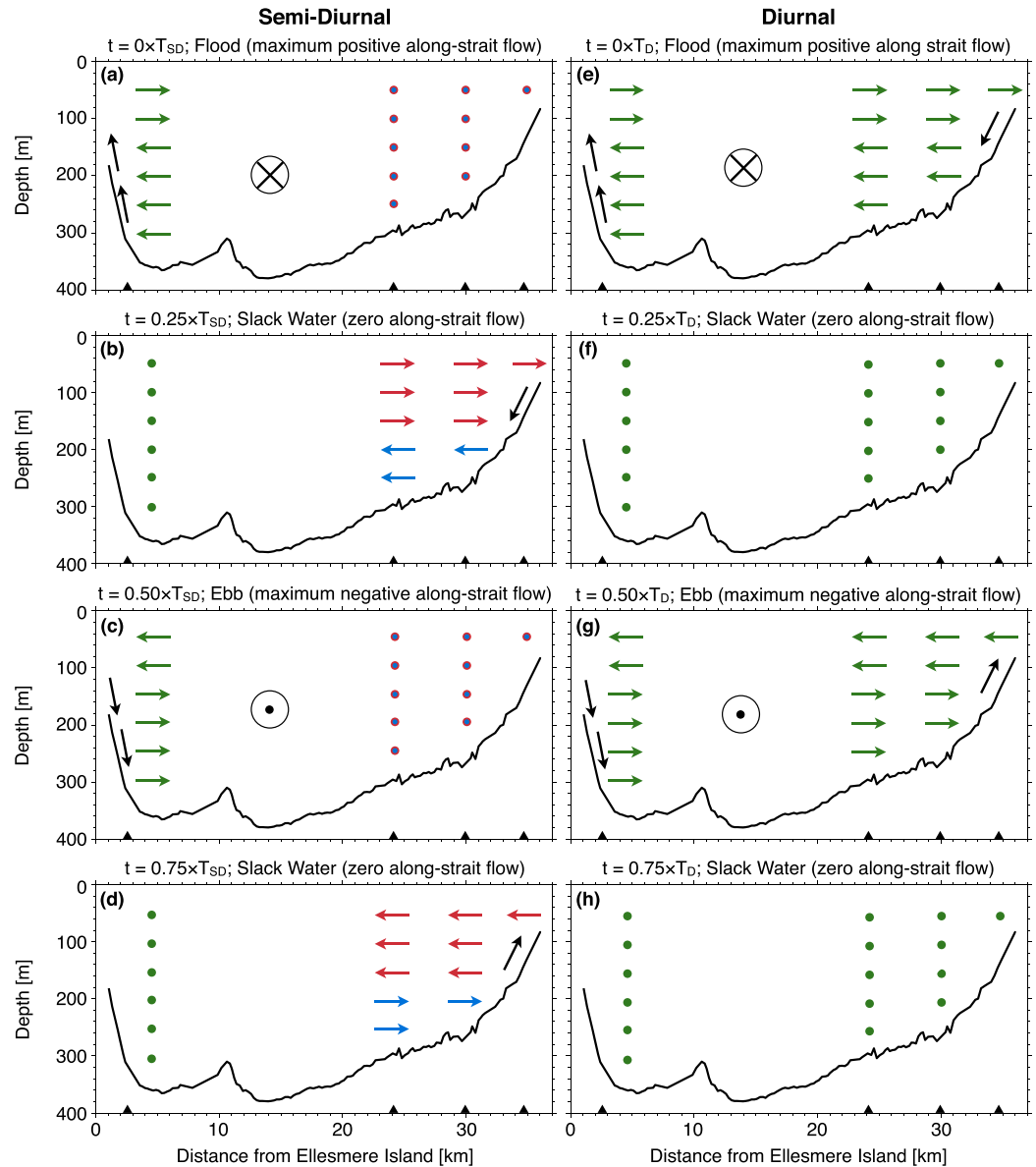


**Figure 11.** Schematic showing the dominant direction of the across-strait tidal flow at each ADCP during the four phases of the semidiurnal tidal cycle: (a) flood (maximum positive along-strait flow); (b) first slack water (zero along-strait flow); (c) ebb (maximum negative along-strait flow); (d) second slack water (zero along-strait flow), and the four phases of the diurnal tidal cycle: (e) flood; (f) first slack water; (g) ebb; and (h) second slack water.  $T_{SD}$  is the period of the semidiurnal tide and  $T_D$  is the period of the diurnal tide. The  $\otimes$  indicates that the diurnal or semidiurnal tidal current vector is at a maximum toward the Arctic at that stage of the tidal cycle, while the  $\odot$  indicates that the diurnal or semidiurnal tidal current vector is at a maximum toward Baffin Bay. Blue arrows indicate the direction of the across-strait flow at depths where clockwise rotation of the tidal current vector is observed, red arrows indicate the direction of the across-strait flow at depths where counterclockwise rotation of the tidal current vector is observed, and green arrows indicate the direction of the across-strait flow at depths where the tidal current vector is rectilinear. Dots indicate periods of zero across-strait flow. Black arrows indicate the direction of the flow up and down the slope adjacent to Ellesmere Island and Greenland.

driven by the interaction of the across-strait tidal flow with the steeply sloping side wall of Ellesmere Island. The across-strait flow driven by the highly rotational tidal ellipses in the center of Nares Strait converges at KS02, and substantial vertical motion is generated as the rotation of the rectilinear tidal ellipses away from the along-strait direction drives a flow against the steeply sloping side walls. This vertical motion (along with that at KS12 which is a quarter of a period out of phase) likely drives significant variability in the density field at tidal time scales, and contributes to maintaining continuity in the across-strait direction.

## 5.2. Schematic of Across-Strait Tidal Circulation

Figure 11 summarizes the important aspects of the across-strait tidal flow during the four phases of both the semidiurnal and diurnal tidal cycle: flood (maximum positive along-strait flow; Figures 11a and 11e), first slack water (zero along-strait flow; Figures 11b and 11f), ebb (maximum negative along-strait flow; Figures 11c and 11g), and second slack water (Figure 11d,h). In general, the semidiurnal across-strait flow shows a two-layer structure with a phase lag of approximately a quarter of a tidal cycle between flow on the two sides of the strait, while the diurnal tide shows the same two-layer structure but without the phase lag.

At  $t = 0 \times T_{SD}$  or  $t = 0 \times T_D$  (i.e., flood; Figures 11a and 11e), the semidiurnal or diurnal tidal current vectors are at a maximum toward the Arctic, with amplitudes as seen in Figure 6 (red lines). At KS02, the across-strait flow for both the diurnal and semidiurnal tide is dominated by a rotation of the ellipse inclination angle, and thus the across-strait flow is at a maximum. Water is moving toward Ellesmere Island below 100 m (ellipse inclination angles  $>60^\circ$ ; Figure 7), and there is significant upward vertical motion due to the steeply sloping bathymetry. Above this, the ellipse inclination angles are generally  $<60^\circ$ , and water is moving toward Greenland. At KS10, KS12, and KS14, the semidiurnal across-strait flow is dominated by a fattening of the tidal ellipse, and therefore, the across-strait flow is small at this point of the tidal cycle (dots in Figure 11a). In contrast, for the diurnal tides, rotation of the tidal ellipse dominates the across-strait flow throughout Nares Strait, and thus the diurnal across-strait flow is at a maximum everywhere.

A quarter of a semidiurnal or diurnal tidal cycle later (i.e.,  $t = 0.25 \times T_{SD}$  or  $t = 0.25 \times T_D$ ), the along-strait flow is close to zero. For the diurnal tide everywhere in Nares Strait, and for the semidiurnal tide against Ellesmere Island, the across-strait flow is zero due to the rectilinear nature of the tidal currents (Figures 11b and 11f). Away from Ellesmere Island, the semidiurnal across-strait flow is at a maximum and reflects the same pattern seen at KS02 a quarter of a cycle earlier. At depths where clockwise rotation of the tidal current is observed (red arrows), water is moving toward Greenland, while at depths characterized by counterclockwise rotation (blue arrows), water is moving toward Ellesmere Island.

At the midpoint of the tidal cycle ( $t = 0.50 \times T_{SD}$  or  $t = 0.50 \times T_D$ ; Figures 11c and 11g), the semidiurnal or diurnal tidal current vectors are at a maximum toward Baffin Bay. The two-layer structure throughout Nares Strait in the diurnal across-strait flow and at KS02 in the semidiurnal across-strait flow reverses, with water moving toward Ellesmere Island above 100 m (driving a significant vertical motion down the steeply sloping bathymetry), and toward Greenland below this. At KS10, KS12, and KS14 the semidiurnal across-strait flow is small, as the tidal ellipses are aligned with the along-strait direction and the across-strait flow is dominated by a fattening of the tidal ellipse.

A quarter of a tidal cycle later, however, at the second slack water (i.e.,  $t = 0.25 \times T_{SD}$  or  $t = 0.25 \times T_D$ ), the across-strait semidiurnal flow at KS02 and the diurnal flow everywhere has come to a rest, while the clockwise rotation of the semidiurnal tidal current vector in the upper water column moves water toward Ellesmere Island, and the counterclockwise rotation of the semidiurnal tidal current vector in the lower water column moves water toward Greenland (Figures 11d and 11h). Finally, after a full diurnal or semidiurnal tidal period, the diurnal and semidiurnal tidal current vectors are pointing again toward the Arctic, and the cycle in the tidal flow through and across Nares Strait begins again.

## 6. Summary and Implications

The primary goal of this paper has been a descriptive analysis of the tidal currents in Nares Strait in terms of their propagation and vertical variability. We have observed that the barotropic semidiurnal tides form a standing wave in Nares Strait, resulting in significantly stronger tides than would be found in a progressive tidal wave regime. Observation-model comparisons show that only the most recent generation of barotropic tidal models can recreate the standing wave behavior we observe.

This result has important implications when using tidal models in studies that explore, for example, the flow dynamics through Nares Strait, or the wider rapid environmental change that is occurring throughout the Arctic Ocean. Indeed, as tidal mixing has been shown to have climatically important impacts by modifying the distribution of temperature and salinity throughout the water column (Holloway & Proshutinsky, 2007; Luneva et al., 2015), it is critical to use state-of-the-art tidal models that accurately resolve the propagation of individual barotropic tidal waves, as well as their interaction with topography that lead to vertical mixing through benthic stresses and shear instabilities in the generated baroclinic tides. By mixing heat to the surface, tides exert an important influence on the sea ice budget in the CAA and the wider Arctic Ocean (Holloway & Proshutinsky, 2007; Luneva et al., 2015; Rippeth et al., 2015), while vertical tidal mixing of salinity and density may also place an important constraint on the magnitude of the freshwater flux exiting the Arctic Ocean. Surface tidal currents are also important for the horizontal movement and fracturing of Arctic sea ice (Kowalik & Proshutinsky, 1994). Thus, the strong tidal currents in Nares Strait are likely to be important for the formation/breakup of the landfast ice bridges that form to the north and south of the region in the Lincoln Sea and Smith Sound (Figure 1; Melling, 2000). As the last of the reservoir of thick, multiyear Arctic sea ice that drains through Nares Strait is replaced with a new, thinner Arctic sea ice type (Ryan & Münchow, 2017), the balance between wind stress, tide stress, and ice stress that controls the formation of the landfast ice bridges (Rallabandi et al., 2017) may be altered to such an extent that ice bridges either no longer form, or only form sporadically. An example of such an event was observed between 2007 and 2009, with an associated 65% increase in the total freshwater export through Nares Strait (Münchow, 2016; Shroyer et al., 2015).

The existence of semidiurnal standing waves in Nares Strait and the large sea surface height tidal amplitudes (Figure 2) is, however, a geographic coincidence. The formation of these standing waves relies on the progressive semidiurnal tidal waves found to the north in the Arctic Ocean interacting perfectly with the similarly progressive semidiurnal tidal waves found to the south in Baffin Bay. On geological time scales, if continental rearrangements or the evolution of local or remote ice sheets closed off Nares Strait, or altered the phase and/or energy of the progressive tidal waves in the Arctic Ocean and Baffin Bay, then tides in the region would be substantially different. Indeed, both Griffiths and Peltier (2009) and Wilmes and Green (2014) have shown that Arctic tides during the Last Glacial Maximum were considerably stronger, with enhanced tidal dissipation and mixing due to internal waves. However, Nares Strait was closed due to the presence of the Laurentide Ice Sheet, with substantial impacts on the Arctic freshwater budget. Nevertheless, when the Laurentide Ice Sheet retreated between 9,000 and 8,000 years ago, strong tides reappeared in Nares Strait (Wilmes & Green, 2014), likely due to the establishment of semidiurnal standing waves in the region. Wilmes and Green (2014) have also shown that present day Nares Strait tides are sensitive to the position of the Antarctic ice sheet grounding line in the Ross and Weddell seas, since this affects the position of the amphidromic points in the North Atlantic. Therefore, any climatically induced future changes in the position of these grounding lines (e.g., Hellmer et al., 2017) may have significant remote impacts on the tidal circulation and freshwater budget in Nares Strait and the wider Arctic Ocean.

Our results have shown that there are significant variations both in the vertical structure of the tides geographically across Nares Strait and between the different diurnal and semidiurnal tidal constituents. While a full analysis of the dynamics that set the vertical structure of the tides is beyond the scope of this study, aspects of this variability are similar to observations made in Antarctica (Makinson et al., 2006) and elsewhere in the CAA under landfast ice (Prinsenber & Bennett, 1989). These similarities suggest that proximity of Nares Strait to the semidiurnal critical latitude and friction in the bottom and under-ice boundary layers (Prandle, 1982) are likely playing leading-order roles in setting the vertical structure of the tides. The critical latitude effects can account for the depth-invariant nature of the diurnal tides compared to the depth-dependent nature of the semidiurnal tides, as well as the substantial differences in the shape of the tidal ellipses. Significant divergences from the vertical structure that would be expected from critical latitude effects alone are observed, however, suggesting that other dynamical processes are also important. In the upper water column, where stratification is important, there is evidence to suggest that phase-coherent baroclinic activity is enhancing tidal current amplitudes by up to 25%, and the steep side wall of Ellesmere Island places a strong topographical restriction on the flow. Here there is significant vertical displacement over each tidal cycle, with likely impacts for the horizontal density gradients found closer to the surface (Rabe et al., 2010; Shroyer et al., 2015). This vertical motion may well be responsible for the phase-coherent baroclinic activity that is observed in the upper water column. Furthermore, by modulating the strength of these density gradients over each tidal cycle, the tides may be driving a residual transport and a net movement of freshwater through the region,

impacting the importance of Nares Strait in the pan-Arctic freshwater budget (Beszczynska-Möller et al., 2011; Curry et al., 2014).

This study has built upon our existing knowledge of tidal flow in Nares Strait (Chen et al., 2009; Münchow & Melling, 2008), raising additional questions regarding the dynamics responsible for controlling the observed structure of the tides, and the long-term net effect that tidal dynamics may have on the freshwater flux through the region. Given the climatic importance of understanding the mechanisms that control the freshwater flux through Nares Strait and the wider CAA, it is of critical importance that future studies aim to understand these high-frequency tidal dynamics.

#### Acknowledgments

We would like to acknowledge and thank Andreas Münchow for his invaluable contribution to the funding, deployment, and recovery of the ADCP instrument array in Nares Strait. We thank the officers and crew of USCGC Healy and CCGS Henry Larsen for all their hard work during deployment and recovery. We also thank technicians Peter Gamble, Jonathan Poole, Ron Lindsay, and Dave Huntley, whose capabilities were essential to the field component of this Canadian Arctic Through-flow Study. Funding for the operations of and capital equipment needed for this work was provided by the National Science Foundation (grant OPP-0230236) and by the Canadian Department of Fisheries and Oceans—staff, institutional support, and logistical infrastructure. H. L. J. and P. D. were funded by the Natural Environment Research Council, grant NE/H01988X/1. We are also grateful for the comments from Laurie Padman and two anonymous reviewers that significantly improved the manuscript. The data used in this study can be found at <https://arcticdata.io/catalog/#view/doi:10.5065/D698854C>, and the TPX08-atlas data can be downloaded from [http://volkov.oce.orst.edu/tides/tpx08\\_atlas.html](http://volkov.oce.orst.edu/tides/tpx08_atlas.html).

#### References

- Agnew, T. A. (1998). Drainage of multiyear sea ice from the Lincoln Sea. *Canadian Meteorological and Oceanographic Society Bulletin*, *26*, 101–103.
- Becker, J. J., Sandwell, D. T., Smith, W. H. F., Braud, J., Binder, B., Depner, J., et al. (2009). Global bathymetry and elevation data at 30 arc seconds resolution: SRTM30\_PLUS. *Marine Geodesy*, *32*, 355–371.
- Beszczynska-Möller, A., Woodgate, R., Lee, C., Melling, H., & Karcher, M. (2011). A synthesis of exchanges through the main oceanic gateways to the Arctic Ocean. *Oceanography*, *24*, 82–99.
- Chen, C., Gao, G., Qi, J., Proshutinsky, A., Beardsley, R. C., Kowalik, Z., et al. (2009). A new high-resolution unstructured grid finite volume Arctic Ocean model (AO-FVCOM): An application for tidal studies. *Journal of Geophysical Research*, *114*, C08017. <https://doi.org/10.1029/2008JC004941>
- Codiga, D. L. (2011). Unified tidal analysis and prediction using the UTide Matlab functions. Graduate School of Oceanography, University of Rhode Island.
- Copland, L., Mueller, D. R., & Weir, L. (2007). Rapid loss of the Ayles ice shelf, Ellesmere Island, Canada. *Geophysical Research Letters*, *34*, L21501. <https://doi.org/10.1029/2007GL031809>
- Cummins, P. F., Cherniawsky, J. Y., & Foreman, M. G. G. (2001). North Pacific internal tides from the Aleutian Ridge: Altimeter observations and modeling. *Journal of Marine Research*, *59*, 167–191.
- Curry, B., Lee, C. M., Petrie, B., Moritz, R. E., & Kwok, R. (2014). Multiyear volume, liquid freshwater, and sea ice transports through Davis Strait, 2004. *Journal of Physical Oceanography*, *44*, 1244–1266.
- Doodson, A. T. (1921). The harmonic development of the tide-generating potential. *Proceedings of the Royal Society A: Mathematical, Physical and Engineering Sciences*, *100*, 305–329.
- Dushaw, B. D., Howe, B. M., Cornuelle, B. D., Worcester, P. F., & Luther, D. S. (1995). Barotropic and baroclinic tides in the Central North Pacific Ocean determined from long-range reciprocal acoustic transmissions. *Journal of Physical Oceanography*, *25*(4), 631–647.
- Egbert, G. D., & Erofeeva, S. Y. (2002). Efficient inverse modeling of barotropic ocean tides. *Journal of Atmospheric and Oceanic Technology*, *19*, 183–204.
- Foldvik, A., Gammelsrød, T., Nygaard, E., & Østerhus, S. (2001). Current measurements near Ronne ice shelf: Implications for circulation and melting. *Journal of Geophysical Research*, *106*, 4463–4477.
- Foldvik, A., Middleton, J. H., & Foster, T. D. (1990). The tides of the southern Weddell Sea. *Deep Sea Research*, *37*, 1345–1362.
- Foreman, M. G. G. (1977). Manual for tidal heights analysis and prediction (Pacific Marine Science Report 77-10). Patricia Bay: Institute of Ocean Sciences.
- Foreman, M. G. G. (1978). Manual for tidal currents analysis and prediction (Pacific Marine Science Report 78-6). Patricia Bay: Institute of Ocean Sciences.
- Foreman, M. G. G., & Henry, R. F. (1989). The harmonic analysis of tidal model time series. *Advances in Water Resources*, *12*, 109–120.
- Godin, G. (1972). *The analysis of tides*. Toronto: University of Toronto Press.
- Greisman, P., Grant, S., Blaskovich, A., & van Hardenburg, B. (1986). Tidal propagation measurements in Baffin Bay, Lancaster Sound, and Nares Strait. Canadian Contractor Report of Hydrography and Ocean Sciences No. 25, Bedford Institute of Oceanography.
- Griffiths, S. D., & Peltier, W. R. (2009). Modeling of polar ocean tides at the Last Glacial Maximum: Amplification, sensitivity, and climatological implications. *Journal of Climate*, *22*, 2905–2924.
- Haine, T. W. N., Curry, B., Gerdes, R., Hansen, E., Karcher, M., Lee, C., et al. (2015). Arctic freshwater export: Status, mechanisms, and prospects. *Global and Planetary Change*, *125*, 13–35.
- Hellmer, H. H., Kauker, F., Timmermann, R., & Hattermann, T. (2017). The fate of the Southern Weddell Sea continental shelf in a warming climate. *Journal of Climate*, *30*, 4337–4350.
- Holloway, G., & Proshutinsky, A. (2007). Role of tides in Arctic ocean/ice climate. *Journal of Geophysical Research*, *112*, C04S06. <https://doi.org/10.1029/2006JC003643>
- Huntley, H. S., & Ryan, P. (2018). Wind effects on flow patterns and net fluxes in density-driven high-latitude channel flow. *Journal of Geophysical Research: Oceans*, *123*, 305–323. <https://doi.org/10.1002/2017JC012748>
- Johns, W. E., Baringer, M. O., Beal, L. M., Cunningham, S. A., Kanzow, T., Bryden, H. L., et al. (2011). Continuous, array-based estimates of Atlantic Ocean heat transport at 26.5°N. *Journal of Climate*, *24*, 2429–2449.
- Kowalik, Z., & Proshutinsky, A. Y. (1993). Diurnal tides in the Arctic Ocean. *Journal of Geophysical Research*, *98*, 16,449–16,468.
- Kowalik, Z., & Proshutinsky, A. Y. (1994). The Arctic Ocean tides. In O. M. Johannessen, R. D. Muench, & J. E. Overland (Eds.), *The polar oceans and their role in shaping the global environment, Geophysical Monograph Series* (Vol. 85, pp. 137–158). Washington, DC: American Geophysical Union.
- Kulikov, E. A., Rabinovich, A. B., & Carmack, E. C. (2010). Variability of baroclinic tidal currents on the Mackenzie Shelf, the Southeastern Beaufort Sea. *Continental Shelf Research*, *30*, 656–667.
- Luneva, M. V., Aksenov, Y., Harle, J. D., & Holt, J. T. (2015). The effects of tides on the water mass mixing and sea ice in the Arctic Ocean. *Journal of Geophysical Research: Oceans*, *120*, 6669–6699. <https://doi.org/10.1002/2014JC010310>
- Makinson, K., Schröder, M., & Østerhus, S. (2006). Effect of critical latitude and seasonal stratification on tidal current profiles along Ronne ice front, Antarctica. *Journal of Geophysical Research*, *111*, C03022. <https://doi.org/10.1029/2005JC003062>
- Melling, H. (2000). Exchanges of freshwater through the shallow straits of the North American Arctic. In E. L. Lewis, E. P. Jones, P. Lemke, T. D. Prowse, & P. Wadhams (Eds.), *The freshwater budget of the arctic ocean* (Vol. 70, pp. 479–502). Dordrecht, Netherlands: NATO Science Series: Springer.

- Melling, H., Agnew, T. A., & Falkner, K. K. (2008). Fresh-water fluxes via Pacific and Arctic outflows across the Canadian Polar shelf. In R. R. Dickson, J. Meincke, & P. Rhines (Eds.), *Arctic-Subarctic ocean fluxes: Defining the role of the Northern Seas in climate* (pp. 193–247). Dordrecht, Netherlands: Springer-Verlag.
- Melling, H., Johnston, P. H., & Riedel, D. A. (1995). Measurements of the underside topography of sea ice by moored subsea sonar. *Journal of Atmospheric and Oceanic Technology*, *12*, 589–602.
- Moore, C. N. K. (1973). A technique for the cross spectrum analysis of pairs of complex-valued time series, with emphasis on properties of polarized components and rotational invariants. *Deep Sea Research and Oceanographic Abstracts*, *20*, 1129–1141.
- Münchow, A. (2016). Volume and freshwater flux observations from Nares Strait to the West of Greenland at daily time scales from 2003 to 2009. *Journal of Physical Oceanography*, *46*, 141–157.
- Münchow, A., & Melling, H. (2008). Ocean current observations from Nares Strait to the west of Greenland: Interannual to tidal variability and forcing. *Journal of Marine Research*, *66*, 801–833.
- Münchow, A., Melling, H., & Falkner, K. K. (2006). An observational estimate of volume and freshwater flux leaving the Arctic Ocean through Nares Strait. *Journal of Physical Oceanography*, *36*, 2025–2041.
- Munk, W. H., Zetler, B., & Groves, G. W. (1965). Tidal cusps. *Geophysical Journal of the Royal Astronomical Society*, *10*, 211–219.
- Padman, L., & Erofeeva, S. (2004). A barotropic inverse tidal model for the Arctic Ocean. *Geophysical Research Letters*, *31*, L02303. <https://doi.org/10.1029/2003GL019003>
- Pawlowicz, R., Beardsley, B., & Lentz, S. (2002). Classical tidal harmonic analysis including error estimates in MATLAB using T\_TIDE. *Computers & Geosciences*, *28*, 929–937.
- Prandle, D. (1982). The vertical structure of tidal currents. *Geophysical & Astrophysical Fluid Dynamics*, *22*, 29–49.
- Prinsen, S. J., & Bennett, E. B. (1989). Vertical variations of tidal current profiles in shallow land fast ice-covered regions. *Journal of Physical Oceanography*, *19*, 1268–1278.
- Proshutinsky, A. Y. (1991). Tidal water and ice dynamics in the Arctic Ocean. In *Proceedings of the international conference on the role of the polar regions in global change vol. 1*, Geophysical Institute, University of Alaska Press, pp. 296–303.
- Rabe, B., Johnson, H. L., Münchow, A., & Melling, H. (2012). Geostrophic ocean currents and freshwater fluxes across the Canadian polar shelf via Nares Strait. *Journal of Marine Research*, *70*, 603–640.
- Rabe, B., Karcher, M., Kauker, F., Schauer, U., Toole, J. M., Krishfield, R. A., et al. (2014). Arctic Ocean basin liquid freshwater storage trend 1992–2012. *Geophysical Research Letters*, *41*, 961–968. <https://doi.org/10.1002/2013GL058121>
- Rabe, B., Münchow, A., Johnson, H. L., & Melling, H. (2010). Nares Strait hydrography and salinity field from a 3-year moored array. *Journal of Geophysical Research*, *115*, C07010. <https://doi.org/10.1029/2009JC005966>
- Rallabandi, B., Zheng, Z., Winton, M., & Stone, H. A. (2017). Formation of sea ice bridges in narrow straits in response to wind and water stresses. *Journal of Geophysical Research: Oceans*, *122*, 5588–5610. <https://doi.org/10.1002/2017JC012822>
- Rippeth, T. P., Lincoln, B. J., Lenn, Y.-D., Green, J. A. M., Sundfjord, A., & Bacon, S. (2015). Tide-mediated warming of Arctic halocline by Atlantic heat fluxes over rough topography. *Nature Geoscience*, *8*, 191–194.
- Robertson, R. (2005). Baroclinic and barotropic tides in the Weddell Sea. *Antarctic Science*, *17*, 461–474.
- Ryan, P. A., & Münchow, A. (2017). Sea ice draft observations in Nares Strait from 2003 to 2012. *Journal of Geophysical Research: Oceans*, *122*, 3057–3080. <https://doi.org/10.1002/2016JC011966>
- Samelson, R. M., Agnew, T., Melling, H., & Münchow, A. (2006). Evidence for atmospheric control of sea-ice motion through Nares Strait. *Geophysical Research Letters*, *33*, L02506. <https://doi.org/10.1029/2005GL025016>
- Segar, D. A. (2012). Introduction to ocean sciences (3rd ed.).
- Shroyer, E. L., Samelson, R. M., Padman, L., & Münchow, A. (2015). Modeled ocean circulation in Nares Strait and its dependence on landfast-ice cover. *Journal of Geophysical Research: Oceans*, *120*, 7934–7959. <https://doi.org/10.1002/2015JC011091>
- Smith, W. H. F., & Sandwell, D. T. (1997). Global sea floor topography from satellite altimetry and ship depth soundings. *Science*, *26*, 1956–1962.
- Stroeve, J. C., Serreze, M. C., Holland, M. M., Kay, J. E., Malanik, J., & Barrett, A. P. (2012). The Arctic's rapidly shrinking sea ice cover: A research synthesis. *Climate Change*, *110*, 1005–1027.
- Sverdrup, H. L., Johnson, M. W., & Fleming, R. H. (1942). *The oceans: Their physics, chemistry, and general biology* (pp. 516–604). New York: Prentice-Hall.
- Visbeck, M., & Fischer, J. (1995). Sea surface conditions remotely sensed by upward-looking ADCPs. *Journal of Atmospheric and Oceanic Technology*, *1*, 141–149.
- Wilmes, S.-B., & Green, J. A. M. (2014). The evolution of tides and tidal dissipation over the past 21,000 years. *Journal of Geophysical Research: Oceans*, *119*, 4083–4100. <https://doi.org/10.1002/2013JC009605>
- Woodgate, R. A. (2018). Increases in the Pacific inflow to the Arctic from 1990 to 2015, and insights into seasonal trends and driving mechanisms from year-round Bering Strait mooring data. *Progress in Oceanography*, *160*, 124–154.